Gonçalo Ramos dos Lóios

Licenciado em Ciências de Engenharia Mecânica

Fatigue life assessment of endodontic instruments subjected to multi planar curvature

Dissertação para obtenção do Grau de Mestre em Engenharia Mecânica

Orientador: Prof. Doutor Rui Fernando Martins, Professor Auxiliar, FCT-UNL/DEMI

Júri:

Presidente: Prof. Doutora Rosa Maria Mendes Miranda
Vogais: Prof. Doutor João Mário Burguete Botelho Cardoso
Prof. Doutor Rui Fernando dos Santos Pereira Martins

FACULDADE DE CIÊNCIAS E TECNOLOGIA
UNIVERSIDADE NOVA DE LISBOA

Setembro 2015

Fatigue life assessment of endodontic instruments subjected to multi planar curvature

Acknowledgments

I would like to specially thank my supervisor, Professor Rui Fernando Martins, for providing me with the tools to succeed, motivation and the opportunity to develop such interesting study, and for all that I offer my appreciation.

I would like to express my gratitude to the responsible of the ISQ-NDT laboratory Eng. Hugo Carrasqueira and to the ISQ for providing me the radiographic tests needed do develop my study. Additionally I wish to thank all the ISQ-NDT staff, and especially to the radiographic testing technician Tiago Amoreirinha for the help and time granted.

I also would like to thank the partnership with Faculdade de Medicina Dentária of Universidade de Lisboa and with Transilvania University of Brasov.

I give my gratitude and dedicate this work to my parents Paulo and Maria Lóios who were responsible for the development of my humanity and to my brother Vasco Lóios for all the friendship.

To my dear Inês, my deepest gratitude for the companionship shown during this challenge.

To my family, friends and colleagues who have supported me every step of the way. In special to the future MSc Ricardo Vieira and future MSc Jorge Torres for the support in the form of engineering insight and technical, all was essential to give me the motivation to succeed.

To all of these individuals, I give my deepest gratitude.

Resumo

Este trabalho teve como principal intuito a avaliação da vida à fadiga de instrumentos endodonticos fabricados em NiTi com controlo de memória de refª *Hyflex® CM™* da marca *Coltene™,* em estado original, submetidos à multi curvatura de um canal radicular típico de um primeiro molar mandibular. Adicionalmente foi estudado o respectivo comportamento estrutural através de uma análise não linear pelo método dos elementos finitos (MEF).

Os ensaios experimentais de vida à fadiga foram realizados em doze instrumentos, recorrendo à mesma curvatura do canal radicular usado na análise pelo MEF; nove dos doze instrumentos testados foram sujeitos a *Pecking motion, i.e.* a movimento relativo do tipo axial, e para tal foi usado um modelo produzido em aço inoxidável do mesmo primeiro molar mandibular. O modelo foi fixo num suporte dotado de movimento axial pertencente à montagem experimental projetada especificamente para a realização deste estudo. Adicionalmente, foi confirmada a multi curvatura do modelo através de radiografia.

Foi usado o programa informático de desenho assistido por computador *Solidworks™* para modelar a geometria de um primeiro molar mandibular produzido em aço inoxidável, assim como para fazer a modelação simplificada do instrumento endodôntico em estudo e posterior realização de análises não lineares pelo MEF através do pack *Simulation* incluído no programa supramencionado. Para tal, foi analisada a geometria do canal radicular de um primeiro molar mandibular existente em modelo 3D com o objetivo de definição dos deslocamentos impostos requeridos pelo MEF.

Os resultados experimentais mostraram que os instrumentos sujeitos a *pecking motion* obtiveram um valor médio de vida à fadiga superior aos instrumentos testados apenas com flexão rotativa e apresentaram um segmento de instrumento fracturado de maior dimensão do que os que não foram sujeitos a este tipo de movimento.

Com a realização das análises não lineares pelo MEF foram obtidos valores máximos para a primeira tensão principal inferiores à tensão de cedência do material, localizados em posições equivalentes às onde foi verificada a ocorrência da rotura dos instrumentos pelo método experimental em situações comparáveis.

Palavras-chave: Vida à fadiga, Instrumentos Endodônticos, Canal Radicular com Multi Curvatura, *Pecking motion*, *Laser Additive Technology*.

Abstract

This present study aimed to investigate the fatigue life of unused (new) endodontic instruments made of NiTi with control memory by Coltene™ and subjected to the multi curvature of a mandibular first molar root canal. Additionally, the instrument's structural behaviour was analysed through non-linear finite element analysis (FEA).

The fatigue life of twelve *Hyflex™ CM* files was assessed while were forced to adopt a stance with multiple radius of curvature, similar to the ones usually found in a mandibular first molar root canal; nine of them were subjected to *Pecking motion,* a relative movement of axial type. To achieve this, it was designed an experimental setup with the aim of timing the instruments until fracture while worked inside a stainless steel mandibular first molar model with relative axial motion to simulate the pecking motion. Additionally, the model's root canal multi-curvature was confirmed by radiography.

The non-linear finite element analysis was conducted using the computer aided design software package *SolidWorks™ Simulation,* in order to define the imposed displacement required by the FEA, it was necessary to model an endodontic instrument with simplified geometry using *SolidWorks™* and subsequently analyse the geometry of the root canal CAD model.

The experimental results shown that the instruments subjected to pecking motion displayed higher fatigue life values and higher lengths of fractured tips than those with only rotational relative movement.

The finite element non-linear analyses shown, for identical conditions, maximum values for the first principal stress lower than the yield strength of the material and those were located in similar positions to the instrument's fracture location determined by the experimental testing results.

Keywords: Fatigue Life, Endodontic Instruments, Root Canal with Multi Curvature, Pecking Motion, and Laser Additive Technology.

Contents

Table Index

Figure Index

Abbreviations, Acronyms and Symbols

MEF – Método dos elementos finitos (Finite Element Method)
CAD – Computer Aided Design
FEA – Finite Element Analysis
FCC – Face-Centred Cubic
HCP – Hexagonal Close-packed
DSC – Differential Scanning Calorimeter
VAR – Vacuum Arc Remelting
VIM – Vacuum Induction Melting
SE – Super Elastic
CM – Control Memory
SMA – Shape Memory Alloy
TTR – Transformation Temperature Range
RTTR – Reverse Transformation Temperature Range
HT – Heat Treated
CT – Computed Tomography
ISQ – Instituto de Soldadura e Qualidade
NDT – Non Destructive Testing
PLA – Poly Lactic Acid

Nitinol – *Nickel Titanium-Naval Ordnance Laboratory*
Labend – *Laboratório de ensaios não destrutivos*

Ni – nickel
Ti – titanium
NiTi – Nickel-Titanium alloy
A – austenite
R – rhombohedral
M – martensite
%wt – weight percent
M_s – start for martensite nucleation temperature
M_f – finish of martensite nucleation temperature
R_s – start of R-phase nucleation temperature
R_f – finish of R-phase nucleation temperature
A_s – start of austenite nucleation temperature
A_f – finish of austenite nucleation temperature
σ – stress

T – temperature

ρ – volumetric mass density

$\triangle S$ – change in entropy

ε_0 – initial strain

k – linearity parameter

f_m – volume fraction of martensite transformation

ε_t – transformation strain

ε_t^0 – theoretical limit of transformation strain

σ_{min}– minimum stress

σ_{max} – maximum stress

σ_m – mean component of stress

σ_r – midrange/amplitude component of stress

σ_0 – nominal stress

K_f – fatigue stress concentration factor

K_t – static stress concentration factor

q – notch sensitivity factor

a – crack length

a_i – initial crack length

N – number of cycles

ΔK_1 – Mode-I stress intensity range

C – material constant (coefficient) used in the Paris Law

m – material constant (exponent) used in the Paris Law

K_{1c} – critical stress intensity factor (fracture toughness)

L – lingual

MB – mesiobuccal

DB – distobuccal

r – radius of curvature

1. Introduction

With the occurrence of pulp infection usually the affected tooth needs to be subjected to a *pulpectomy* this is the removal of the pulp tissue, other related organic debris and microorganisms achieved by Endodontic Therapy [1]. The Endodontic Therapy is a multi-stage procedure, during which, in the initial stage, is used a Bur (drilling instrument) to get coronal access, then the root canals are shaped to a tapered form using endodontic files, afterwards the prepared root canal is cleaned with the use of irrigating solutions and finally filled with an inert filling material usually *gutta-percha* [1] .

Endodontic therapists have at their disposal different techniques such as crown-down, step-back, step-down and single length techniques to successfully shape the root canal to a tapered form and clean it from organic debris.

With the step-back technique the point is to create a tapered form root canal by preparing the canal at the full working length in the apical region with master apical files, then shape the canal towards the pulp chamber using successive larger file sizes, each one inserted 1 mm less into the canal, between instrument placement the canal is recapitulated (usage of master apical file to clean the canal) [2]. Contrasting with the step-back technique, the step-down technique starts by enlarging the coronal region of the root canal and then shaping the canal towards the apical region using successive smaller files [2]. One advantageous physical aspect of this technique is that it removes dentinal interferences in the coronal apical two-thirds of the canal, easing the use of apical instrumentation [2]. The initial objective of the crown-down technique is to prepare the coronal region of the tooth by using preparatory and drill types instruments and then continue the preparation using narrower instruments towards the apex. The step-back technique is used to complete the procedure [3].

Some endodontic files manufacturers have their own recommended techniques. For instance Coltene® recommends the single length technique to be used with their *Hyflex™ CM* files [4], the same files that were used in this study. With this technique there isn't a coronal to apical or apical to coronal approach as in the step-down or step-back techniques, instead it's used small file sizes to prepare the root canal from the coronal region to the apex and then the procedure is repeated with a set of larger file sizes as shown in *Figure 1*, noting that the first and second numbers in the upper right corner of the scheme boxes are associated respectively to the taper and diameter 10^{-2} mm of the file tip.

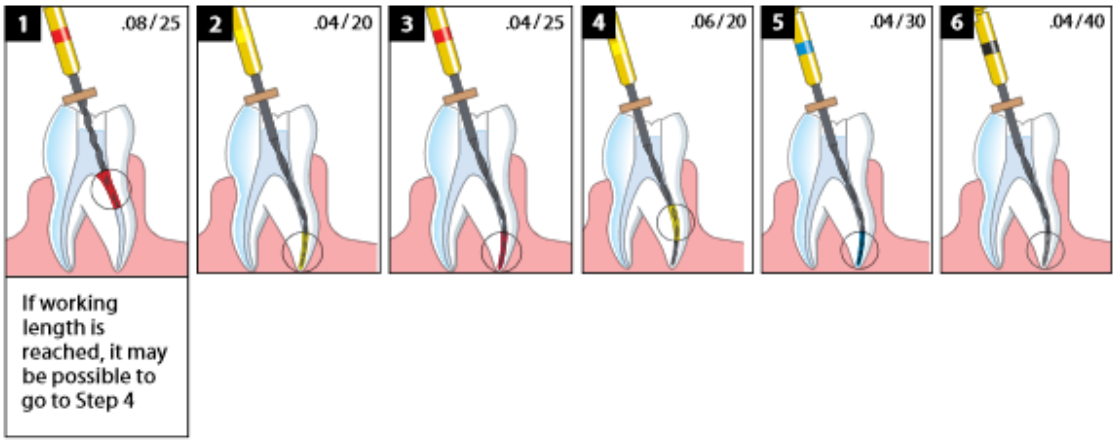

Figure 1.1- Schematic representation of the single-length technique [4]

On a mechanical root canal preparation a micro-motor is used coupled to an endodontic file. The angular speed and torque is recommended by the file manufacturer, NiTi files are refereed as NiTi rotary instrumentation. The single-length technique can only be used when dealing with mechanical root canal preparations, Coltene® recommendations for speed and torque when using *Hyflex™ CM* are 500 rotations per minute and 2.5 N.cm respectively [4].
In addition, there is a technique called Pecking Motion that enhances fatigue life of rotary instrumentation; this technique consists in adding cyclical axial motion to the rotational motion [5].

1.1 NiTi instrumentation

The success of endodontic therapy depends on the root canal morphology. When used to prepare curved root canals, NiTi instruments have the advantage and thus the preference over stainless steel ones, this is due to their greater flexibility, which is caused by the instrument's material properties that allows it to adapt and follow the curvature of the root canal [6].

NiTi instrumentation is usually made of 55-Nitinol (55% Ni wt.) with some variations between manufactures and models *Table 1.1*, as the ratio of Ni Ti is closely related to the instruments properties [6]. Nitinol at near equiatomic ratios can have 3 stress-temperature dependent microstructural phases, austenite, martensite, and R-phase [7]. The literature refers to NiTi instruments as of super-elastic (SE) type or control memory (CM) type depending on which phase they are during clinical use (buccal temperature of 37ºC). Considering this, control memory and super-elastic types instruments will be at their martensitic phase and austenitic phase respectively [7], R-phase type instruments like Twisted Files are at their austenitic phase during clinical use, the R-phase reference comes from the fact that these instruments are

manufactured by twisting and need to be at this phase for mitigate the super elastic properties that would difficult the manufacturing process. [7], [8].

Table 1.1 - Ni (% wt)of different NiTi instruments [9].

Instrument	Ni (% wt)
Hyflex	52.1
EndoSequence	56
ProFile	54.6
Hero	55.4
FlexMaster	56.2

As depicted on *Figure 1.2*, the total deformation achieved by the (SE) NiTi alloy is greater than the stainless steel. In fact NiTi alloys with super-elastic properties can recover from deformations of as much as 8% strain, while stainless steel will only recover up to 1% [9].

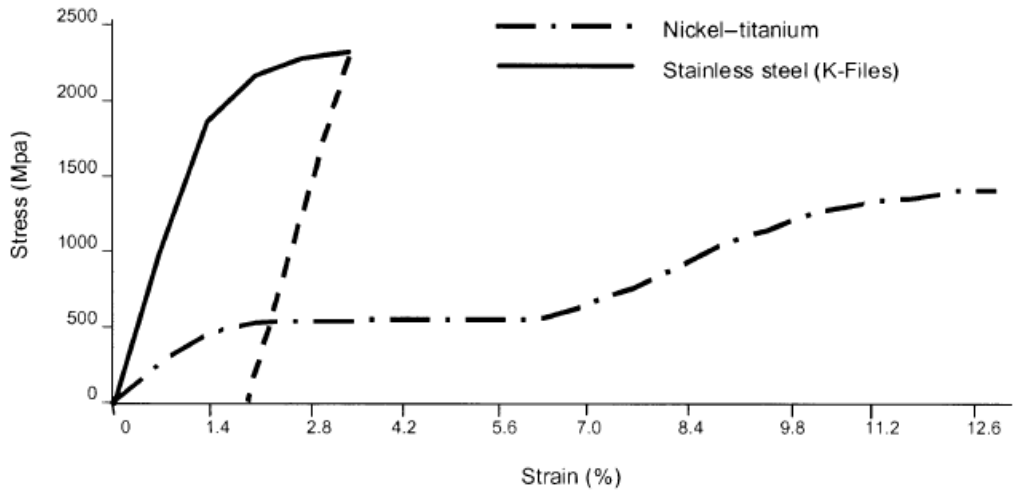

Figure 1.2 - Stress-strain curve: stainless steel and nickel-titanium (SE) [9].

1.2 Nitinol characterization

Nitinol is an acronym related to the material's composition of Nickel Ni, Titanium Ti and Naval Ordnance Laboratory, the place where it was first investigated. Nitinol is also the name given to the family of NiTi alloys. These alloys have the ability to modify their type of atomic bonding and therefore exist in 3 different crystal structures, the monoclinic B19', the B2 cubic and the R rhombohedral lattices corresponding respectively to the martensitic and austenitic depicted in the *Figure 1.3* and the intermediate R-phase. The reason behind the shape memory effect of Nitinol shape memory alloys (SMA) and super elasticity (SE) of near equiatomic NiTi alloys is the diffusion-less structural transition between the monoclinic B19' and the cubic B2 structures [10].

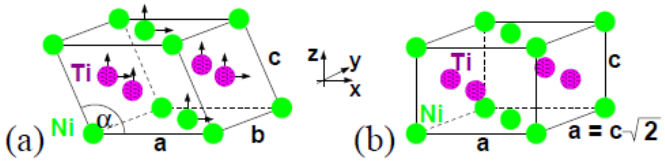

Figure 1.3 - (a) NiTi monoclinic B19' and (b) cubic B2 structures, (lattice constants a,b and c), structure angle α [10].

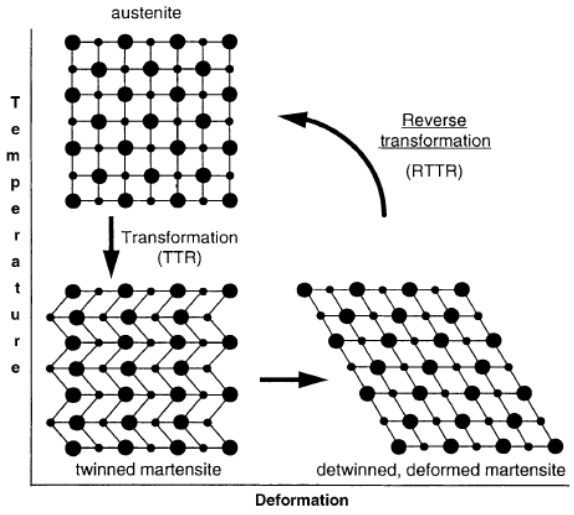

Figure 1.4 - Diagrammatic representation of the martensitic transformation and shape memory effect of NiTi alloy [11].

The austenite to martensite transition, can be stress or temperature induced. When the alloy's temperature decreases through its transformation temperature range (TTR) suffers the transformation shown in the *Figure 1.4* , which is called martensitic transformation and depends on the start of martensite nucleation (M_s) and finish (M_f) temperatures. At (M_S) portions of martensite start to nucleate within the austenite structure creating twin planes that constitute low

energy mobile boundaries in a process known as twinning. The resulting structure at (M_f) is a multiple twin variant martensite B19' structure with twined morphology [12], [13].

The monoclinic B19' lattice low symmetry is the reason why the alloy has greater ductility during the martensitic phase and therefore being easily deformable [10], [11]. The deformation occurred during the martensitic phase can be recovered by inducing a temperature increase over its TTR (Reverse transformation temperature range RTTR) *Figure 1.4*, resulting in the recovery of the cubic B2 lattice arrangement, with an total atomic movement between adjacent planes of atoms being less than a full interatomic distance comparing to the initial austenite lattice, providing the alloy with the pre deformation shape, this is the so called shape memory effect. Additionally the reverse transformation also recovers the original austenite phase properties [11].

The alloy's phase transformations are dependent with the thermo-mechanical history of the alloy, as there is a hysteretic type response to temperature, *Figure 1.5*. Additionally, there is an intermediate third phase called R-phase in accordance to the metallurgical rhombohedral structure with trigonal symmetry. The R-phase is comprised between the martensitic B2 to B19' transition [10].

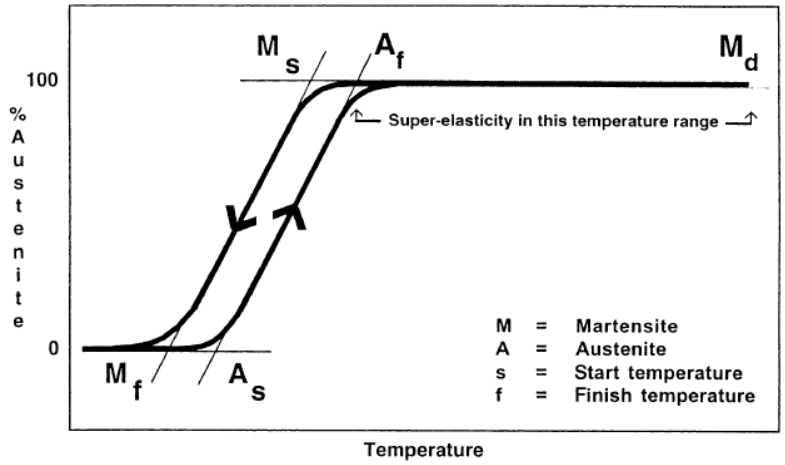

Figure 1.5 - Hysteresis of martensitic transformation [11].

Differential scanning calorimeter (DSC) is a widely used thermoanalytical equipment to assess phase transformation temperatures and enthalpies of transitions. It utilizes a reference sample as control to determine the variation of heat required to increase the temperature of the test sample. Exothermic or endothermic phase transformations will require different amounts of heat appearing in the DSC curves as positive or negative peaks depending on the type of instrument used. K.L. Ng, et al in their study have determined the DSC curves of a SMA/CM NiTi tube (*Figure 1.6*).

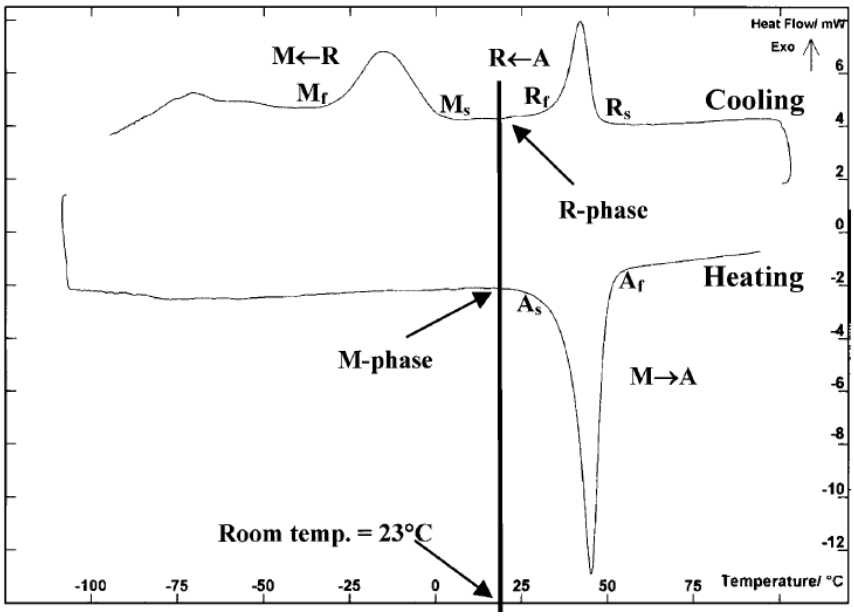

Figure 1.6 - DSC thermogram of SMA/CM NiTi tube [14].

Table 1.2 - Transformation temperatures of the SMA NiTi tube.

R_s	R_f	M_s	M_f	A_s	A_f
52.1 ºC	28.2ºC	5.5ºC	-32.7 ºC	23.3ºC	57.1ºC

Accordingly to the DSC test results shown in *Figure 1.6,* the tube studied could present initial stress-free M or R phases at a room temperature of 23ºC depending on the thermal load applied. By lowering the tube's temperature to less than -100ºC and then heating up, the tube phase transformations would follow the lower DSC curve, keeping an initial M-phase at room temperature and reaching the start of austenite nucleation temperature, A_s at 23.3ºC and the finish of austenite nucleation temperature, A_f at 57.1 ºC. By rising the tube temperature to more than 100ºC and lowering it, the phase transformations would follow the upper DSC curve, reaching the start of R-phase formation at 52.1 ºC and presenting fully formed R-phase at room temperature.

As referred previously, NiTi alloys can also suffer from stress-induced martensitic transformation SIM, concerning NiTi endodontic files, this can occur during root canal preparation [11]. Instead of the occurrence of mechanical slip within the lattice structure, NiTi with an initial A or R structure response to an external force resulting in a stress that surpasses a certain critical value is the occurrence of a mechanical twinning mechanism that causes the nucleation and growth of twin variants of the monoclinic (B19') structure, this mechanism is known as the stress-induced martensitic transformation and relies on the shear strain. This dependence on the shear strain may be the reason why the critical stress for the SIM transformation of NiTi with initial A structure is greater than one with an initial R structure as the R-phase possesses lower shear modulus than the martensite and austenite structures [15]. The twinned martensite overall structure is a combination of multiple variants of the monoclinic (B19') structure self-accommodated in a twinned morphology resulting in a lower energy state [12]. With additional load applied resulting in the shearing of the twinned variants, one twin variant will grow at expense of the others in a process known as detwinning, forming a detwinned martensite structure *Figure 1.4*.

Contrary to most metals, the super elastic (SE) characteristic of NiTi is the result of the ability to recover from deformations as much as 8% when there isn't the occurrence of mechanical slip within the detwinned martensite structure [11].

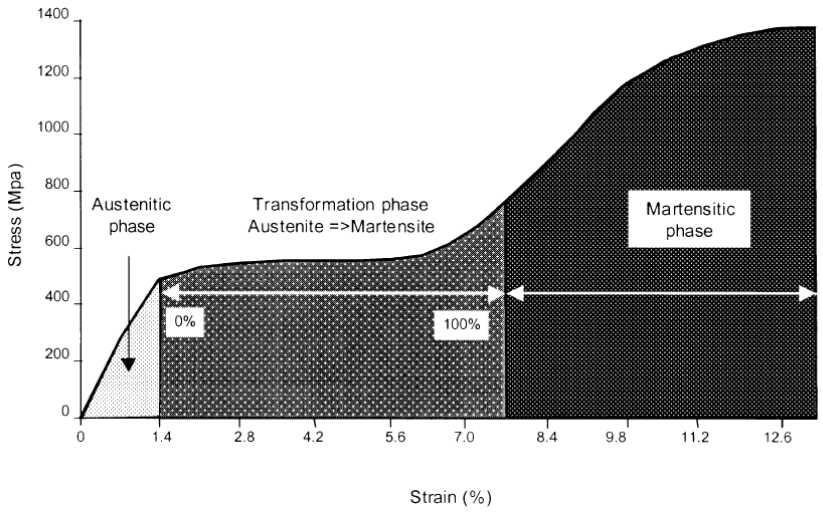

Figure 1.7 - Stress-induced martensitic transformation and martensite detwining.

As known and referred earlier, the phase transformations of Nitinol are stress/temperature induced. The relationship between phase transitions, the stress and temperature can be simplified for a given temperature range with a Clausius-Clapeyron type relation [16]. The adapted Clausius-Clapeyron relation to an equation, characterizes a discontinuous phase transition between two phases, in the stress vs temperature phase diagram it will give the slope of the tangents of the coexistence curve. For a complete phase transformation with incomplete transformation strain orientation, as would occur during stage III, *Figure 1.7* (Martensitic detwinning), Yinong Liu and Hong Yang [16] suggested the following equation.

$$\frac{\partial \sigma}{\partial T} = -\frac{\rho \Delta S}{\varepsilon_0} \frac{1}{1 + 2k\sigma} \qquad (1)$$

For an incomplete phase transformation with proportional completeness degree of transformation strain orientation, as would happen during a stress induced martensitic transformation shown as the stage II in the *Figure 1.7* the suggested equation would be the following (Eq.2).

$$\frac{\partial \sigma}{\partial T} = -\frac{\rho \Delta S f_m}{\varepsilon_t} \qquad (2)$$

The current transformation strain (ε_t) is proportional to the volume fraction of martensite transformation, (f_m). The theoretical limit of the transformation strain (ε_t^0) is achievable when the transformation is complete ($f_m = 1$).

$$\varepsilon_t = \varepsilon_t^0 f_m \qquad (3)$$

The *Figure 1.8* is referent to a near equiatomic Nitinol and shows the linear relation between stress and temperature on the R to M structure transformation (upper curve) and on the M to A reverse transformation (lower curve). The M to A reverse transformation can be achieved either by unloading or heating the alloy as shown in the heating curve of the *Figure 1.6* or a combination of both processes. The R to M forward transformation can be achieved by stressing the alloy (stress induced martensitic transformation) or cooling the alloy as depicted on the cooling curve of the *Figure 1.6* or also as combination of both processes

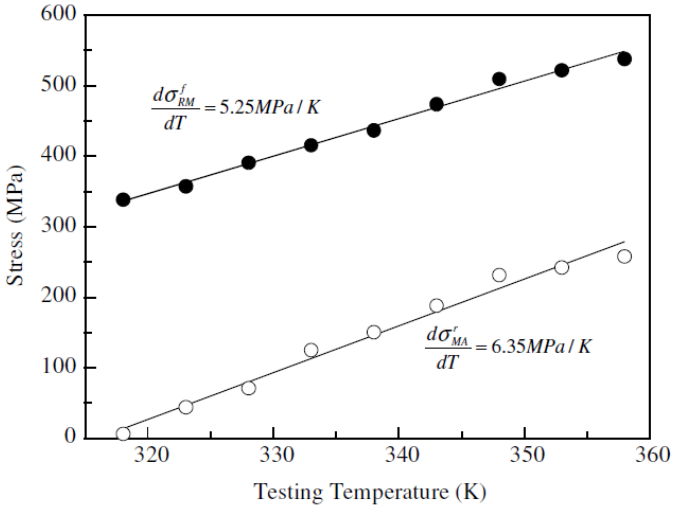

Figure 1.8 - Temperature relation with the critical stresses for the R - M forward transformation and M - A reverse transformation [16].

.

K.L. Ng, Q.P Sun in their studies have determined a different phase diagram with the temperature dependence of transformation stress on NiTi polycrystalline shape memory alloy tubes with 54.1 at.% Ni *Figure 1.9*. The critical stress of transformation for A to R, A to M and R to M increased with temperature, there was a slight deviation from linearity of the Clausius-Clapeyron relation for the A to R transformation at low temperatures in accordance to other studies [14],[16]. It is important to note that with the increase of temperature the two-stage phase transformation, A to R and R to M transformed into a single stage transformation A to M, this goes in line with the already stated unpredictability of R phase appearance in some alloys.
With no load applied the process governing the phase transformations is temperature dependent and it follows the DSC heating and cooling curves of the same SMA NiTi tube in the *Figure 1.6* , the points of transformation temperatures in the *Figure 1.9* are the same as in the *Figure 1.6*.

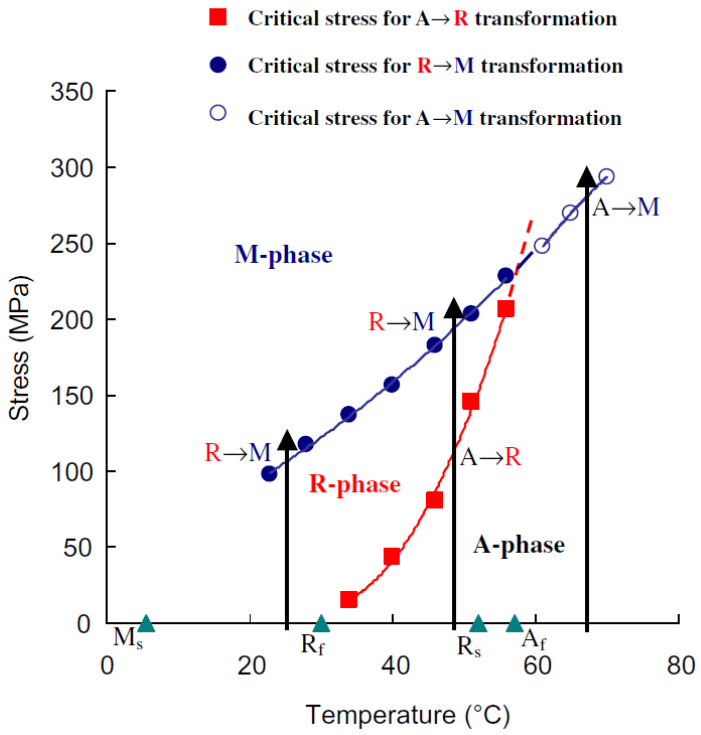

Figure 1.9 - Temperature relation with the critical stresses of transformation of an SMA NiTi tube [15].

It's known by experimental and molecular-dynamics simulation results that Ni concentration in NiTi alloys has a considerable influence on the transformation temperatures [10]. Considering that the ground structures of pure Ni and Ti are respectively face centred cubic (FCC) and hexagonal close packed (HCP) structures, they differ from the higher cohesive energy B19' martensitic structure. With the increase of either one of the components, there will be greater quantity and size of pure material pockets energetically affecting the overall structure and the effect of reduced cohesive energy is closely related to the decrease of transformation temperatures [10].

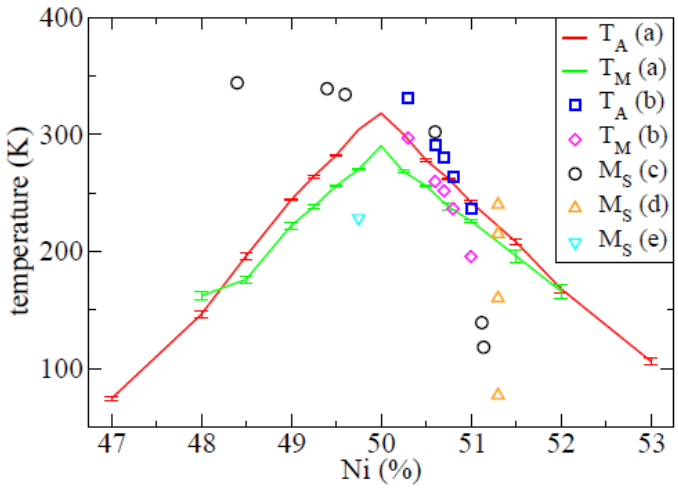

Figure 1.10 - Dependence of the transition temperatures on Ni concentration. Simulated data (a) , experimental values (b,c,d and e) [10].

Since the transformation temperatures are of extreme importance for the desirable applicability of the NiTi alloy, the manufacturing process mirrors this importance in the constituent's concentration control.

1.3 Production of Nitinol wires

The influence of the Ni Ti ratio on the phase transformation temperatures and the high reactivity of titanium justify the need for extreme compositional and environmental control during the NiTi wires manufacturing process. Manufacturing of Nitinol ingots consists in melting high purity 94% titanium and nickel components at a specific ratio. The melting process can be either by vacuum arc melting (VAR) *Figure 1.12* or vacuum-induction melting (VIM) *Figure 1.11*.

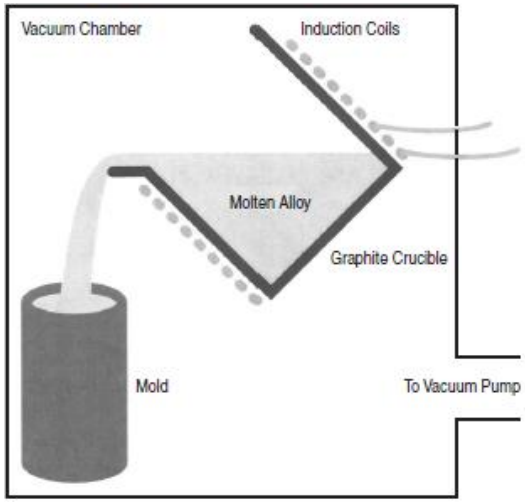

Figure 1.11 - Vacuum-induction melting process [11].

VIM ingots are made by melting the nickel and titanium components inside an electrically conductive graphite crucible. The crucible is heated by the electrical induction coils that surround it exteriorly; as the melting pool begins to form there is a stir effect created by the induction fields. The stir effect is essential to improve the homogeneity of the material and thus the uniformity of transformation temperatures. To counteract the high reactivity of titanium, all the process happens inside a vacuum chamber. The downside of VIM is the possibility of contamination of the molten Nitinol by carbon from the graphite crucible.

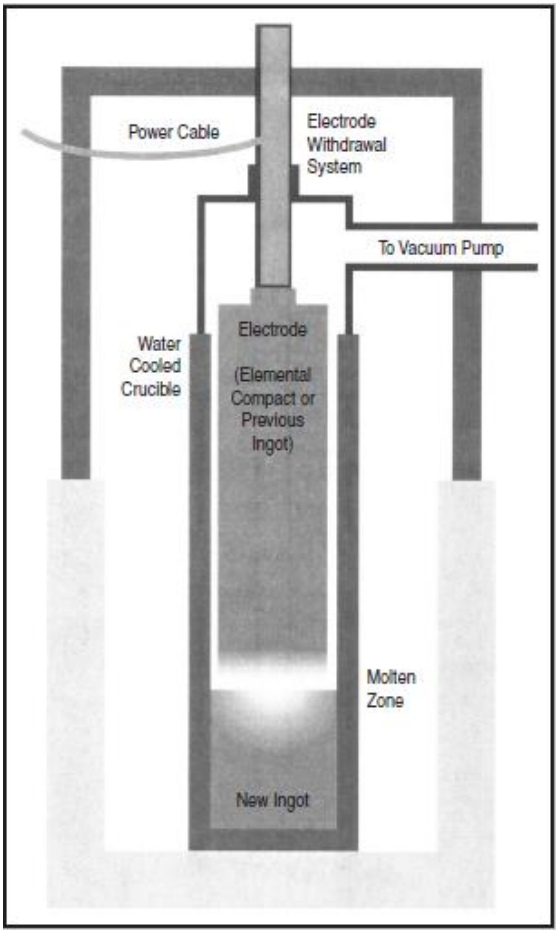

Figure 1.12 - Vacuum arc melting process [11].

VAR ingots are made by mixing and compacting the Ni and Ti components inside water cooled cooper crucible allowing a contamination free molten pool. The melting process happens by creating an electrical arc between the electrode used to compact the mixture and the bottom of the crucible, because there is no stir effect like in the VIM and the time at which the ingot is molten is different, there is the necessity to realize consecutive remelts to achieve acceptable homogeneity. This process can also be used to refine VIM ingots.

Further processes consist in reducing the diametral size of the ingots through hot working processes at temperatures of 600 ºC to 900 ºC. VIM and VAR ingots usually have 50 *cm* in diameter and are reduced to a diameter suitable to be further processed into the final product, usually less than 15 *cm*. To reduce even further the diametral size, further processing is needed, consisting in a series of cold-working and annealing steps. The ingot is cold drawn to successive smaller diameters, reaching more or less 1 mm in diameter for the final wire. Due to the fast work hardening effect and the increasing ultimate tensile strength, the obtained cold drawn NiTi wire needs to be fully annealed at 600ºC to 800ºC as required. Additionally to the enhanced mechanical properties, the cold working processes provide the final product shape and surface finish [11].

1.4 Mechanical properties of NiTi wires

1.4.1 Phase transformation temperatures effect on the mechanical properties of NiTi wires

There are three types of NiTi wires, SE, R and CM, which are produced to be the manufacturing base material of endodontic rotary instrumentation. Each type displays different mechanical properties in accordance with the different metallurgical structures present at ambient temperature. SE DSC test results (*Table 1.3* and *Figure 1.13*) corroborate the super elastic nature of the wires as they usually display a predominant austenite structure at an oral temperature of 37 ºC contrary to CM type wires that usually have a mixture of martensite and R-phase.

It's well known that the Ni Ti ratio can have a considerable effect on the dislocation of the transformation temperature ranges. Some studies [15] that were made to determine the constitution of CM and SE wires concluded that both were nickel rich, the SE wires had nickel content of 50.8% ± 0.7% and the CM wires had 50.7% ± 0.5%. Considering that phase transformation temperatures can decrease with the increase of nickel content in a nickel rich NiTi alloy, some studies suggested this as the reason of the lower A_f temperature of CM wires, although Zhou et al concluded in their study [15] that the different phase transformation temperatures and mechanical properties between SE and CM wires are attributed to the special heat treatment history resulted from the manufacturing processes.

Table 1.3 - Phase transformation Temperatures and Associated Energy from DSC plots for Raw NITI Wires [15].

Type	M_s (ºC)	M_f (ºC)	A_s (ºC)	A_f(ºC)	$\Delta H_{heating}$ (J/g)	$\Delta H_{cooling}$ (J/g)
25SE	21.2 ± 2.7	-1.1 ± 2.6	-21.2 ± 1.6	23.6 ± 2.3	1.6 ± 1.4	-1.9 ± 0.5
48SE	26.4 ± 4.1	2.3 ± 1.9	-14.6 ± 2.1	31.0 ± 3.6	2.1 ± 2.2	-3.8 ± 0.7
25CM	21.3 ± 3.4	-32.1 ± 2.3	20.8 ± 3.2	54.3 ± 4.2	16.7 ± 1.7	-6.9 ± 1.3
48CM	24.2 ± 2.5	-29.1 ± 3.5	25.0 ± 2.7	48.8 ± 3.9	16.4 ± 1.2	-15.7 ± 0.9

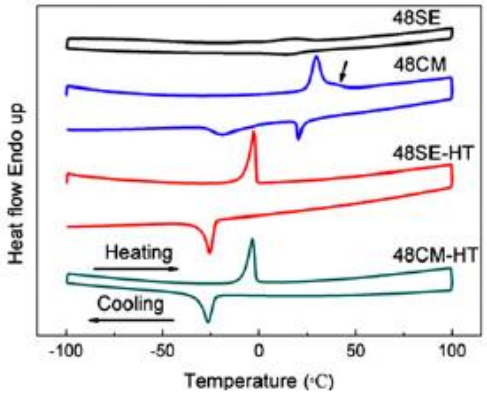

Figure 1.13 - DSC curves of raw and heat-treated (HT) SE and CM wires [15].

1.4.2 55-Nitinol Thermal and Mechanical properties during the Austenitic and the Martensitic Phases

The thermal and mechanical properties of the 55-Nitinol are resumed in the following tables.

Table 1.4 – 55-Nitinol; Austenitic and Martensitic Phases, Thermal Properties [17].

Thermal Properties	55-Nitinol Austenite	55-Nitinol Martensite
Specific Heat Capacity (J/g-ºC)	0.320	0.320
Thermal Conductivity (W/m-K)	10.0	10.0
Melting Point (ºC)	1240 - 1310	1240 - 1310
Solidus (ºC)	1240	1240
Liquidus (ºC)	1310	1310

Table 1.5 - 55-Nitinol; Austenitic and Martensitic Phases, Mechanical Properties [17].

Mechanical Properties	55-Nitinol Austenite	55-Nitinol Martensite
Tensile Strength, Ultimate (MPa)	754 – 960	754 - 960
Tensile Strength, Yield (MPa)	560	100
Elongation at Break (%)	15.5	15.5
Modulus of Elasticity (GPa)	75.0	28.0
Poisson's Ratio	0.30	0.30
Shear Modulus (GPa)	28.8	10.8

1.4.3 SE wires mechanical properties

Superelastic wires characterized by having an initial austenitic structure at room temperature, have stress-strain curves similar to the example in the *Figure 1.7*, composed of an initial elastic stage with an approximate modulus of elasticity of 75.0 GPa followed by a SIM transformation plateau at an approximate critical transformation stress of 560 MPa. The detwinning process of the martensite structure precedes the mechanical slip within the structure that would cause unrecoverable deformation. Further loading resulting in an approximate maximum stress of 960 MPa would cause the wire's rupture [15],[17].

1.4.4 CM wires mechanical properties

The initial structure at room and oral temperature of CM wires is a combination of M and R phases and small portions of A [15]. This specific structure composition with (50,7 %wt ± 0,5%wt Ni) affects the tensile stress-strain response of the CM wire, the *Figure 1.14* shows the stress-strain response of SE and CM wires for two different diameters, 0.64 and 1.22 mm shown respectively as 25 and 48, during loading-unloading process at room temperature, the maximum stress for all the stress-strain curves is the final yield stress *; in fact,* there is an initial elastic response to tensile stress applied characterized by having a modulus of elasticity ranging between the martensite 28,0 GPa to the austenite 75,0 GPa, and further loading leads to a stress plateau that is resultant of martensite reorientation. From this point forward the mechanical response is very similar to the SE wires response, with detwinning process of the martensite structure preceding the mechanical slip within the structure when the final yield stress is surpassed, followed by the final wire rupture at a maximum stress of 960 MPa [15],[17].

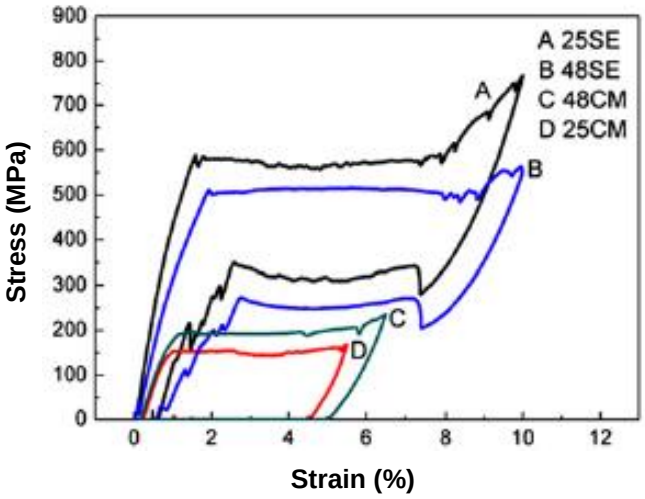

Figure 1.14 - Tensile stress-strain response of SE and CM wires during loading-unloading process performed at room temperature [15].

1.5 Manufacturing of NiTi rotary instrumentation

The manufacturing methods have great influence on the performance and durability of the endodontic files [8]. Although each manufacturer had developed and optimized their own methods and kept them as an industrial secret, there are two well-known main methods, namely grinding *Figure 1.15* and twisting *Figure 1.16* with the possibility of subsequent superficial treatments.

Ground instruments are created by grinding a Nitinol wire in a helical grinder that is fed by a Nitinol spool, the wire is forced against a grinding wheel while rotating.

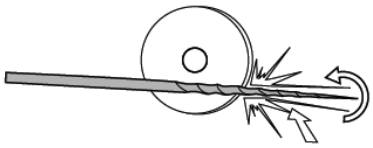

Figure 1.15 - Schematic representation of manufacturing an endodontic instrument through grinding.

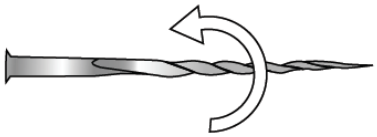

Figure 1.16 - Schematic representation of manufacturing an endodontic instrument through twisting.

Some studies were made about the influence of the different manufacturing methods on the cyclic fatigue of NiTi rotary instrumentation. The conclusions made were that instruments manufactured by twisting had more resistance to low-cycle fatigue ($< 10^4 cycles$) than the ground ones [8].

There are many variables affecting the low-cycle fatigue life, although some are solely related to the manufacturing methods.

The execution of heat treatments prior to shaping or forming the instruments flutes can directly affect the fatigue life of the instrumentation, Twisted files are subjected to a process of heating and cooling forming a molecular structure known as R phase, this phase attributes the NiTi wire with the flexibility required to be twisted. [8]

1.6 Defects

There are defects associated with the manufacture of NiTi rotary instrumentation that can compromise their durability and cutting efficiency. These defects can be surface irregularities such as machining marks in the cutting edges and machining grooves on the flutes (Figure 1.17), presence of debris and pitting, [9][18]. Internal defects such as holes and inclusions are due to the manufacturing process of the NiTi wire used to manufacture the instrument.

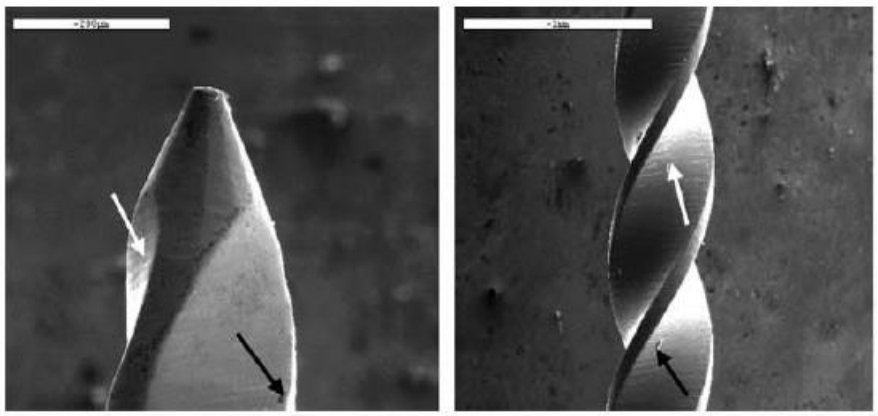

Figure 1.17 - Non cutting tip (original magnification 200 x) and active part (orginal magnification 75 x) of an Profile instrument on the left and right images respectively [18].

In the *Figure 1.17*, considering the left image there are present metal stripes (white arrow) and pits (black arrow). considering the right image there are also metal stripes (white arrow) and adhered material (black arrow) distributed along the surface of the file.

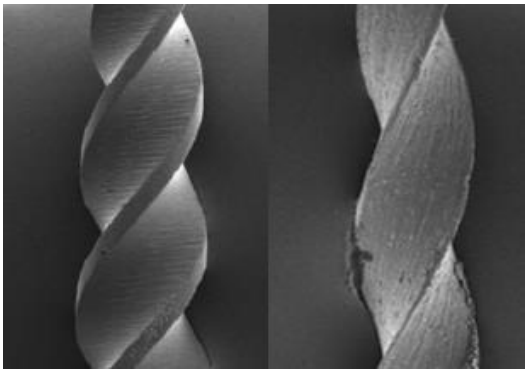

Figure 1.18 - Lateral SEM views of two NiTi instruments flutes. From left to right, Profile and TF files [19].

Contrary to twisted files, ground files like the Profile™ in the *Figure 1.18* present machining defects originated from the grinding process such as machining grooves and other surface flaws like surface debris. The machining defects are mainly superficial but can act as starting points for the propagation of fissures. TF™ files made by twisting lack machining grooves, instead they present wrinkle like grooves longitudinally along the flutes *Figure 1.18* [19]. The presence of superficial defects can be mitigated with surface treatments. The *Figure 1.19* shows the inner defects present on two other files' types, inclusions (black arrows) and voids (white arrows).

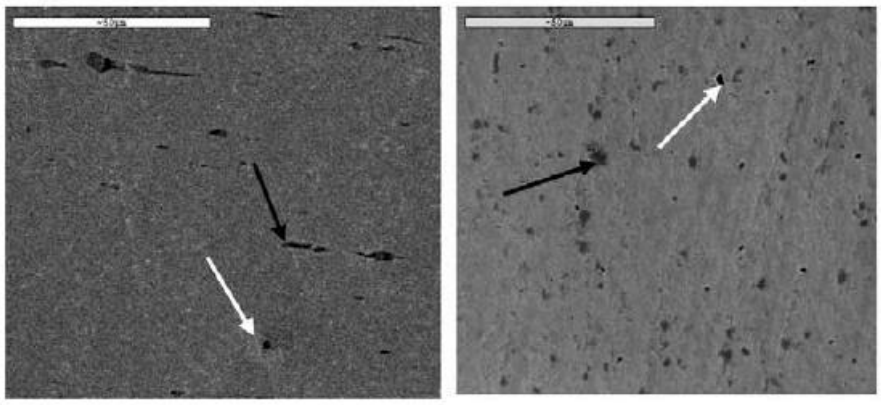

Figure 1.19 - Longitudinal section of a ProFile file and cross-section of a Flexmaster file on the left and right images respectively [18].

1.7 Fatigue Life

The mechanical response of machined components subjected to time-varying loading is of great importance as the nature of the loading creates stresses that vary or fluctuate over time, which can ultimately result in the failure of the part due to fatigue. The fluctuating stresses associated to machine components, which are subjected to rotation usually display a sinusoidal distribution pattern; other components subjected to different loadings modes will present different stress-time relations. In the *Figure 1.20* are represented some stress-time relations for a specific monitored location of a part : (a) fluctuating stress with high frequency ripple, (c) non sinusoidal fluctuating stress, (d) sinusoidal fluctuating stress, (e) repeated stress or (f) completely reversed sinusoidal stress.

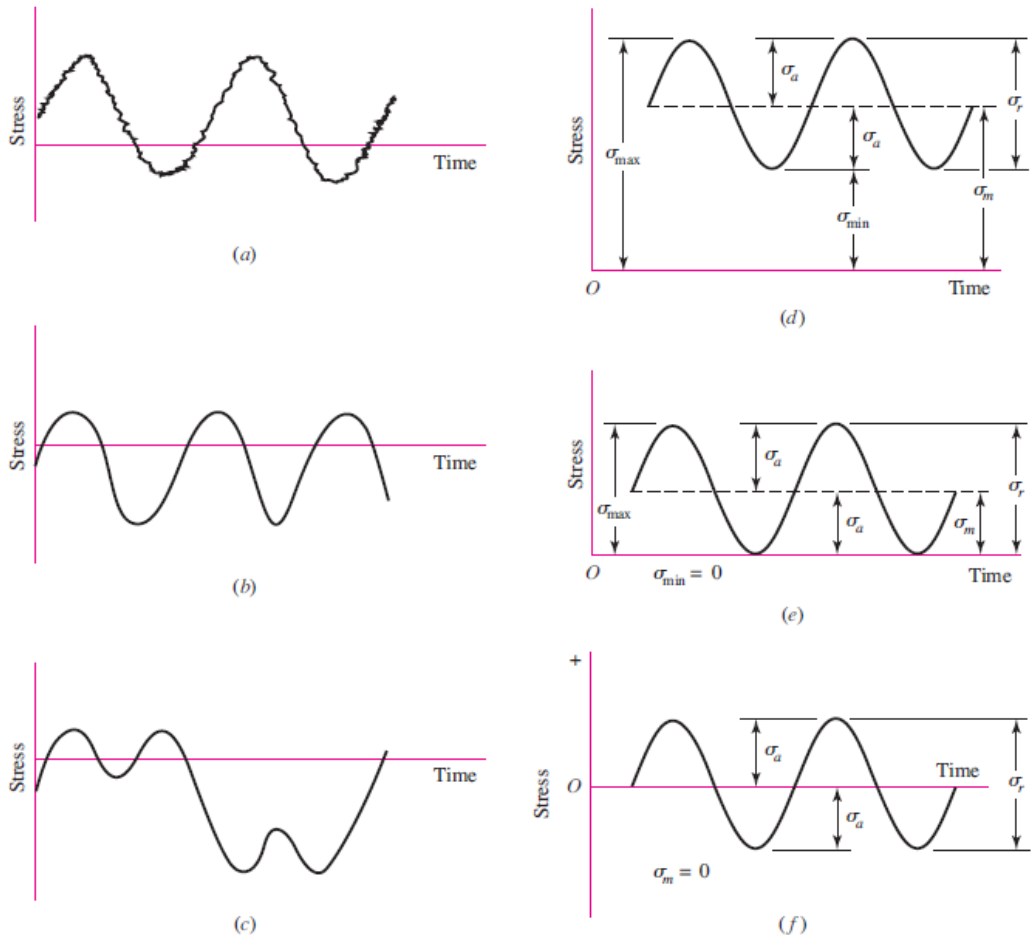

Figure 1.20 - Stress-time relations [20].

In the previous figure (figure 1.20 d) are displayed the following components of stress, minimum stress σ_{min}, maximum stress σ_{max}, amplitude component σ_a, midrange/mean stress component σ_m and load range σ_r. It is possible to define some stress relations based on the stress components (Eqs. 4 and 5).

$$\sigma_m = \frac{\sigma_{max} + \sigma_{min}}{2} \qquad (4)$$

$$\sigma_a = \left|\frac{\sigma_{max} - \sigma_{min}}{2}\right| \qquad (5)$$

Fatigue failure happens without the average magnitude of the stresses surpassing the ultimate strength or even the yield strength of the material. Contrary to static failure, where plastic deformation is evident prior to rupture, fatigue failure happens in a sudden way resulting in total rupture, without any evident warning. The fracture surfaces are much similar to a static brittle fracture, appearing in a planar form type and perpendicular to the first principal stress axis and without the existence of necking. Fracture by fatigue is the end result of three stages of

development. In the first stage, single or multiple micro cracks are formed at discontinuities or stress concentration points, such as material voids, holes, grooves and notches, due to the occurrence of plastic strain when locally the stress level exceeds the elastic limit of the material, and the formed cracks usually will expand about two or five grains in length about the origin.
The reason why crack formation happens at discontinuities and stress concentration points is because stress levels are locally increased by the presence of such features, the maximum resulting stress which can surpass the yield strength of the material, is defined by the product of the nominal stress σ_0 and the fatigue stress concentration factor K_f .

$$\sigma_{max} = K_f \, \sigma_a \qquad (6)$$

$$\Delta\sigma = \sigma_{max} - \sigma_{min} \qquad (7)$$

The fatigue stress-concentration factor K_f is defined for a specific specimen by the relation between the maximum stress in a notched equivalent specimen and the stress in the notch-free equivalent specimen, it is similar to the stress-concentration factor K_t but with lessened sensitivity to notches. The notch sensitivity factor *q* can assume values between 0 and 1 representing respectively the material without notch sensitivity, $K_f = 1$ or full notch sensitivity, $K_f = K_t$ and is defined by the equation.

$$q = \frac{K_f - 1}{K_t - 1} \qquad (8)$$

The second stage consists in the micro cracks propagation to macro cracks. Starting from an initial crack with length value of a_i, its growth for a specific type of loading will be in function of the number of stress cycles N, stress range and in the geometry, size and shape of the crack, which is the stress intensity range ΔK_{I}, the constant β is obtained from tables available in the literature.

$$\Delta K_{\mathrm{I}} = \beta \, \Delta\sigma\sqrt{\pi \, a} \qquad (9)$$

The rate of crack growth (Figure 1.21) during this stage can be approximated by the *Paris equation*.

$$\frac{d\,a}{d\,N} = C(\Delta K_{\mathrm{I}})^m \qquad (10)$$

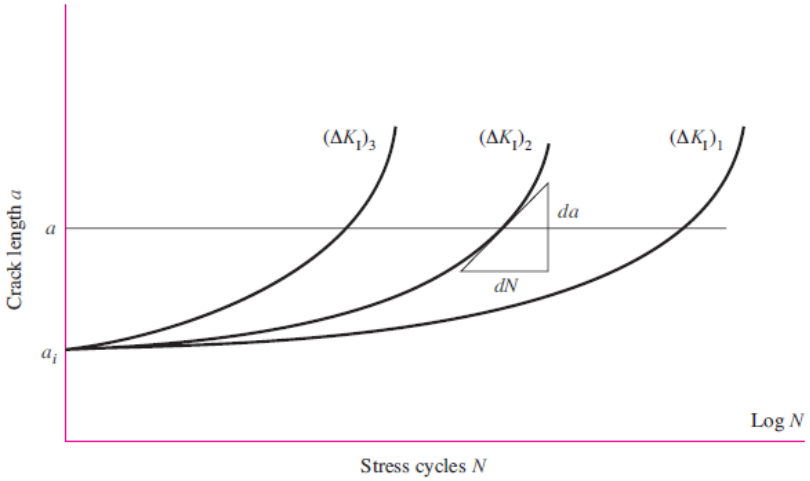

Figure 1.21 - Crack length a growth as function of the number of stress cycles for three different stress ranges [20].

The third stage is characterized by a sudden and catastrophic rupture thus, components subjected to load cycles require caution during the design stage and suitable inspections during the life cycle. The rupture happens in a certain final load cycle when the developed crack is large enough so that $K_1 = K_{1c}$, K_{1c} being the critical stress intensity for the uncracked portion of the material (toughness or fracture toughness). In the *Figure 1.22* is shown as example, the result of fatigue failure of a bolt due to repeated cycles of extension and compression created by unidirectional bending, the crack initiated at the zone marked as A, in the region marked as B are present beach marks that reveal the crack propagation direction, C marks the fracture surface of the uncracked material that resulted from the third stage.

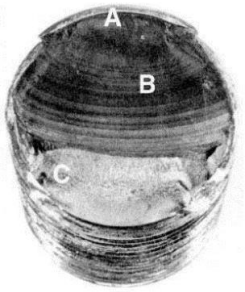

Figure 1.22 - Fatigue failure of a bolt due to repeated unidirectional bending.

Material ruptures can be brittle, ductile or a combination of both [20]. It's possible to assess the type of loading and contributing factors responsible for the fatigue failure by analysing the surface of the fracture *Figure 1.22.*

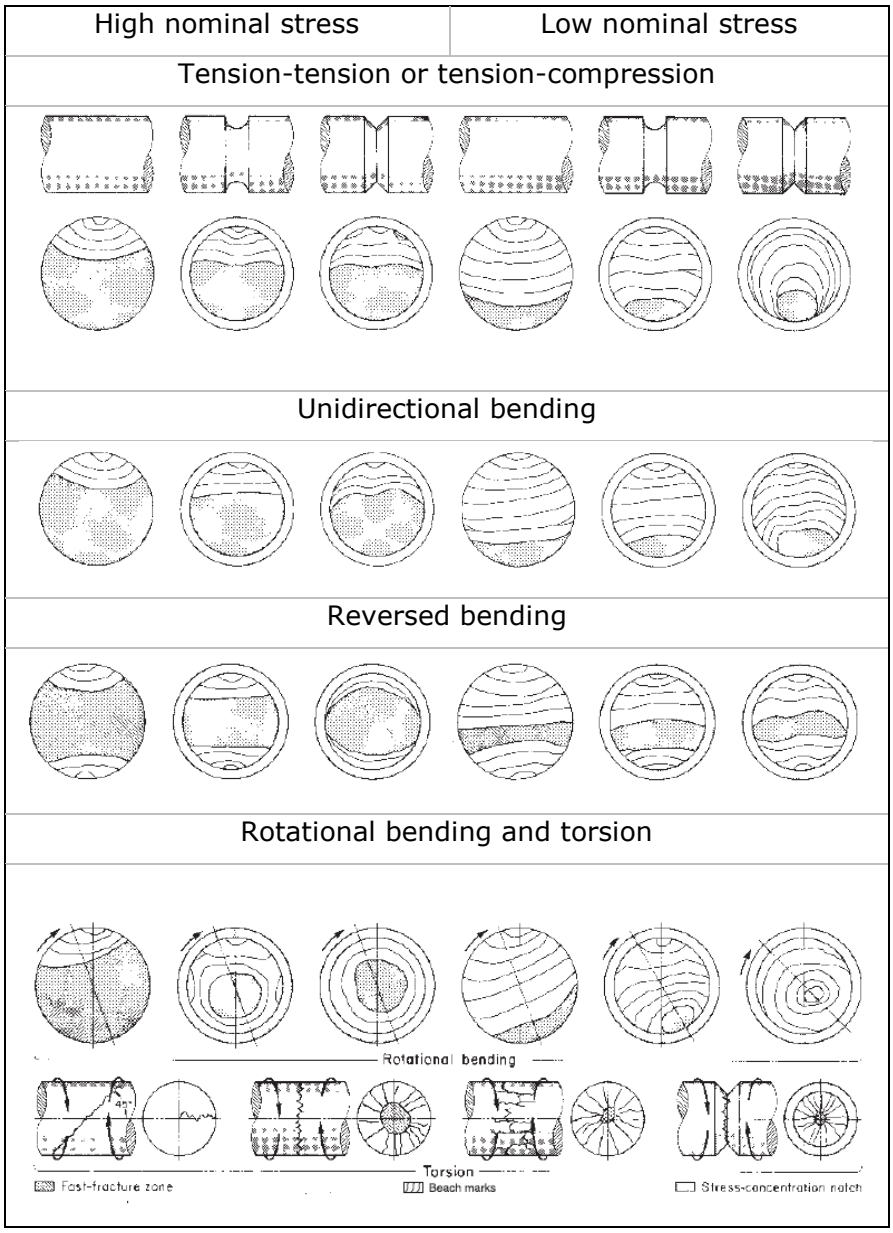

Figure 1.23 - Fatigue surface fractures by different types of load and stress concentration factors [20].

The number of cycles to failure, *N* is an important value to take in consideration when fatigue failure has an important role on the design and analysis of a component. Fatigue failures are categorized by high cycle or low cycle fatigue depending if *N* is respectively higher or lower than $10^3/10^4$ cycles. There are three methods that are commonly used to predict the value of *N* for a specific level of load*, the stress-life method, the strain-life method and the linear-elastic fracture mechanics method.*

The linear-elastic fracture mechanics method is useful to predict the crack growth with respect to stress intensity of an already identified crack, therefore is more commonly used when dealing with large components or structures where cracks can be detected during periodic inspection programs. Although the applicability to large components puts this method out of this study scope, the crack formation and propagation mechanisms are important to understand the nature of a failure by fatigue.

The strain-life method is considered good for low-cycle applications and it takes into account specific regions where the stresses are high enough to cause plastic deformation and by that attempt to estimate fatigue life.

The most common method of the three is the stress-life method, commonly used for high cycle fatigue applications. The tested material is subjected to a several number of tests, the first test starts from a stress level below the ultimate strength of the material, the subsequent tests are realized at decreasing levels of stress and the results are plotted as an *S-N* diagram on a semi-log or log-log paper *Figure 1.24*.

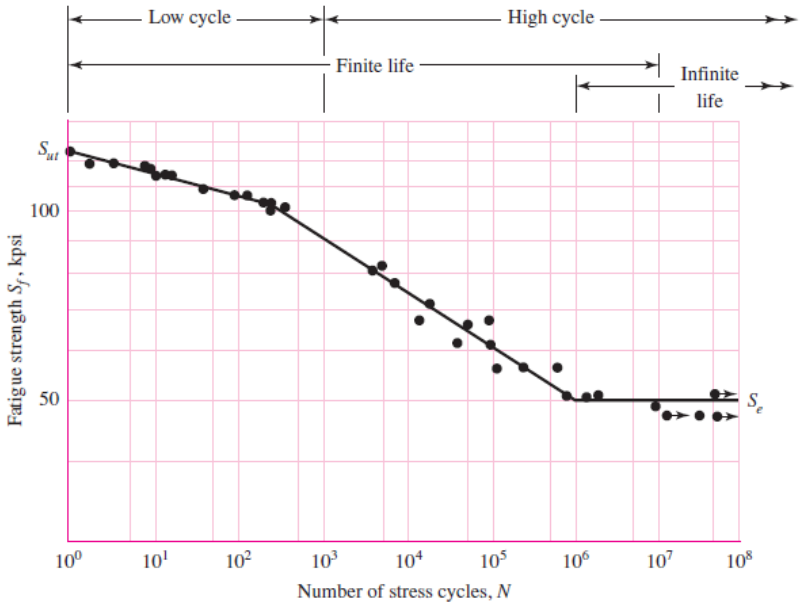

Figure 1.24 - An S-N diagram plotted from the results of completely reversed axial fatigue tests [20].

1.8 Dynamic cyclic fatigue of NiTi rotary instruments

The NiTi rotary instruments capability to follow root canal paths and to adapt to different canal curvatures made them suitable for the endodontic therapy of mandibular and maxillary first molars. Regardless of the clear advantages of such files, file separation can still occur during clinical use as consequence of cyclic, static torsional, and/or dynamic torsional fatigue. "Cyclic fatigue occurs when an instrument is subjected to repeated cycles of compression and tension about the same point, as would occur during rotary instrumentation around a curve" [21]. Static torsional fatigue is the result of an extreme difference in rotational speed between two parts of a file, as would occur when one end of the file becomes locked. During operation, files are subjected to torsion due to frictional forces applied to the file surface; in addition, the cyclic nature of the operation can cause the file separation by dynamic torsional fatigue [21].

Instrument's fatigue life can be decreased by the presence of defects, defects such as milling marks and pits act as starting points for crack nucleation. Fatigue life of NiTi rotary instrumentation can be enhanced by adding relative axial motion between the tooth and the instrument this is referred in the industry and literature as Pecking motion. It's known that highly curved zones correspond to high stress areas, the axial movement provides a varying file position in relation to the referred areas [22].

2. 3D models of Maxillary and Mandibular first molars.

2.1 Modelling the maxillary first molar.

The root canal curvature is an essential characteristic of a tooth that as a major influence on a successful root canal therapy. The two most common teeth to be subjected to therapy are respectively, in order of occurrence, the mandibular first and the maxillary first molars [23]. Tooth root canal curvatures can be decomposed in two distinct directions forming two distinct planes. With the aim of replicating real maxillary first molar roots, it was necessary to create a 3D model using the computer-aided design software Solid Works®.

A study about the morphology of maxillary molars [24], was used to assess the correct proportions and average dimensions of maxillary first molars. In the *Figure 2.1* there is an example of a maxillary first molar with the 3 characteristic and distinct roots, the lingual (L), the mesiobuccal (MB) and the distobuccal (DB).

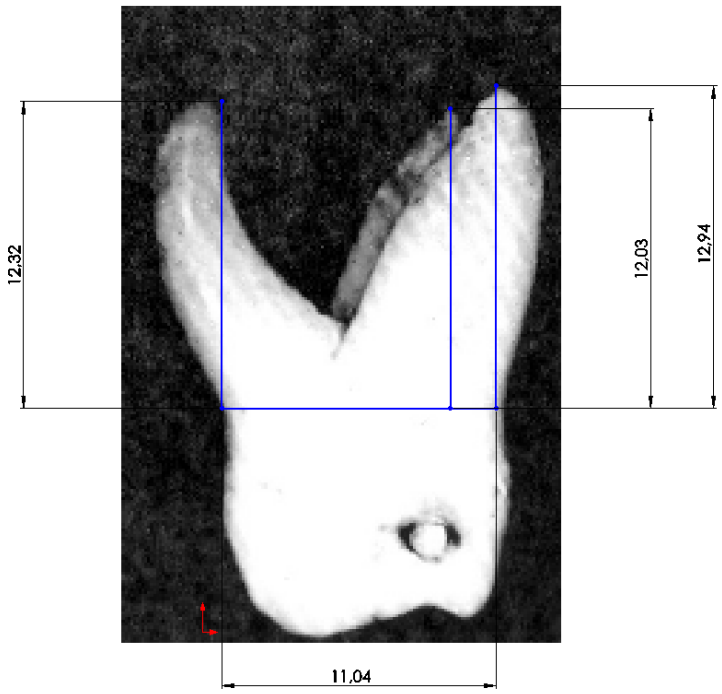

Figure 2.1 - Average dimensions (mm) of a maxillary first molar [23].

The tooth average dimensions are resumed in the *Table 2.1*. For obtaining an accurate model, the most relevant dimension was the distal diameter at cervical line, which was used to give the correct proportion to slice images of a maxillary first molar.

Table 2.1 – Average dimensions (mm) of a maxillary first molar [23].

Tooth length	Distal diameter at cervical line	Lingual root's length	Mesiobuccal root's length	Distobuccal root's length
21.3	11.04	12.32	12.03	12.94

Micro computed tomography microCT is non-destructive scanning technology that utilizes X-ray imaging and computed tomography to produce tomograms (tomographic slice images) of specific objects with high resolution. In teeth morphology and endodontic studies it is commonly used to reveal in great detail the teeth internal structure. Ove A. Peters, Andres Laib ET all in their endodontic study [25] used a microCT system (µCT-20; Scanco Medical, Basserdorf, Switzerland) at 50 kV (cubic resolution 34 µm) to scan maxillary molars and assess changes in the path and cross section area of the root canals before and after endodontic preparation. In the *Figure 2.2* are present the five microCT images used to make the tooth 3D model, the images were chosen from a total of 184 tomograms that ranged from the cervical line to the apex spacing 68 *µ*m between them.

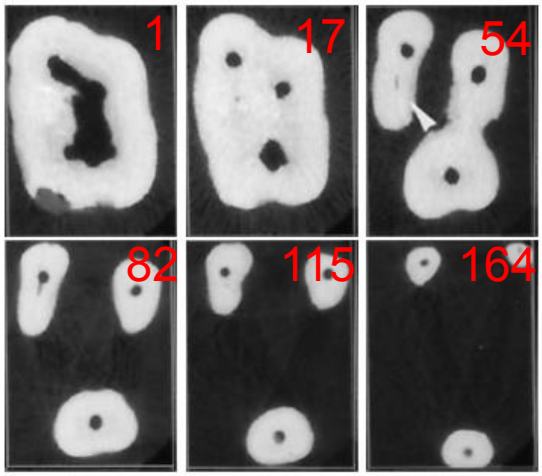

Figure 2.2 - Maxillary first molar µCT slices (numbered in red) ranging from the cervical line (1) to the apical region (164), Note the white arrow identifies the mesiobuccal root [25].

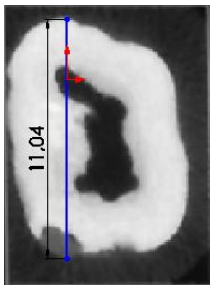

Figure 2.3 - Maxillary first molar µCT slice at cervical line level used to give the correct proportion to the tomograms, dimensions in (mm) [25].

The crossing of the information gathered from the morphology study [24] with the cross-section images of a maxillary first molar present in the endodontic study [25] permitted the accurate 3D modelling of the tooth *Figure 2.4.*

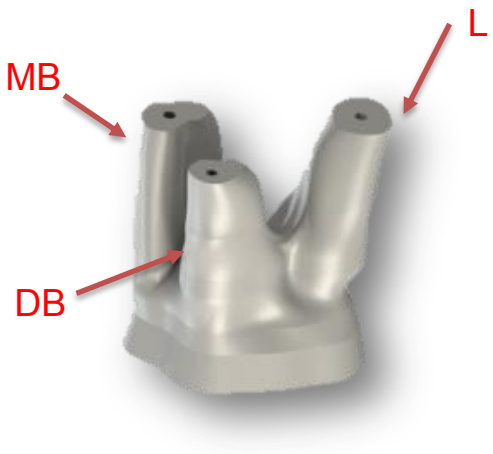

Figure 2.4 - Modelled maxillary first molar with the different roots identified.

Table 2.2 - Maxillary first molar apical exits aproximate diameter per root (*mm*).

Lingual	Messiobuccal	Distobuccal
0.65	0.67	0.57

2.2 Maxillary first molar model

The maxillary first molar model with the replica of the real root canal system was produced in stainless steel to mitigate the effect of possible future corrosion *Figure 2.5*. It was manufactured in the Transilvania University of Brasov recurring to a laser additive manufacturing technology.

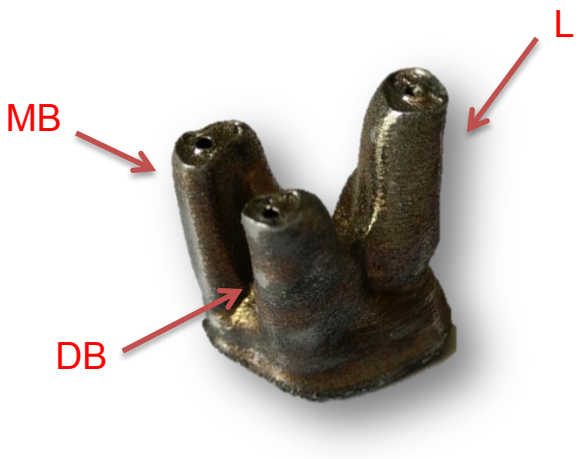

Figure 2.5 - Stainless steel maxillary first molar produced by an addictive manufacturing process, the red arrows indicate the (L) Lingual, (MB) Mesiobuccal and (DB) Distobuccal roots postion.

To correctly assess the root canal system replica existence, non destructive testing was performed in the *Laboratório de Ensaios Não Destrutivos do Instituto de Soldadura e Qualidade* ISQ - LABEND, X-Ray views of the maxillar first molar making 90º between them were taken using an ANDREX™ Constant Potential X-Ray Set *Figure 2.6*.

Figure 2.6 - X-Ray views, courtesy of ISQ-NDT Laboratory.

2.3 Mandibular first molar model

The mandibular first molar model was also produced by an addictive manufacturing technology. The CAD model required for the production was a pre-existent model created by Pedro Santos for his master's dissertation, [26]. The model was created from two perpendicular radiographic views a bucolingual (A) and a mesiodistal (B), and *Figure 2.7* shows a mandibular first molar with a stainless steel instrument inserted to highlight the predicted root canal multi-curvature. The canal displays a primary curvature on the view A and a double curvature on the view B with an upper secondary curvature and a tertiary curvature on the apical region.

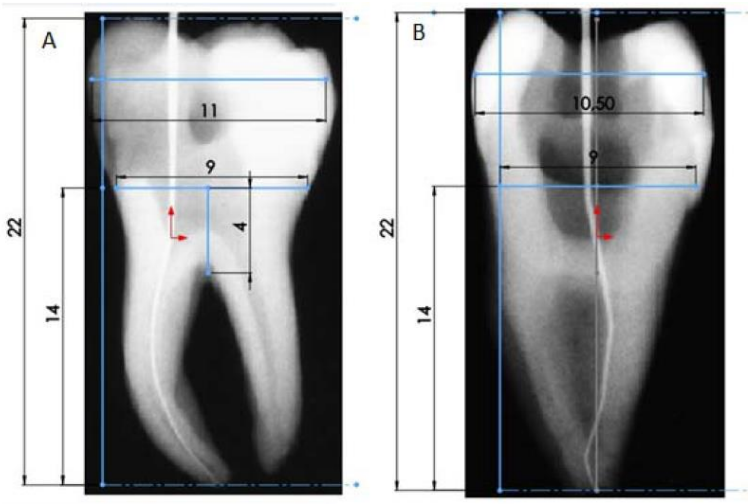

Figure 2.7 – Bucolingual (A) and mesiodistal (B) views of the mandibular first molar[26].

By the identification of the root canal trajectory in both bi-dimensional planes corresponding to the bucolingual (A) and mesiodistal (B) views it was possible to model the mesiobuccal root canal with three dimensional curvatures. The root canal was modelled with a constant diameter of 0.9 mm along the overall path length *Figure 2.8 and Figure 2.9.*

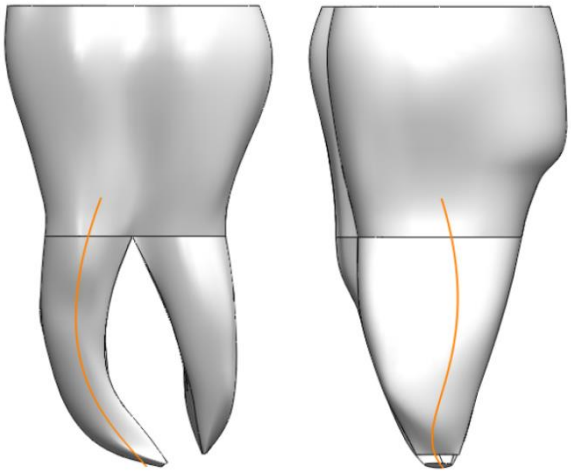

Figure 2.8 – Modelled mandibular first molar with the root canal path highlighted [26].

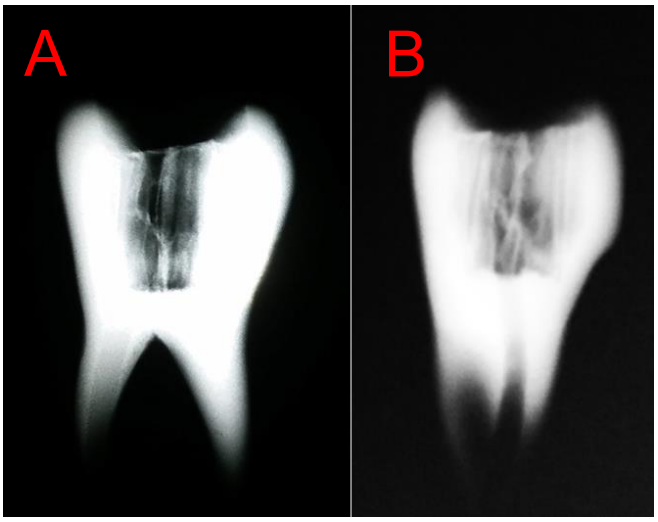

Figure 2.9 – Bucolingual (A) and mesiodistal (B), X-Ray views of the stainless steel mandibular first molar model, courstesy of ISQ NDT-Laboratory.

The mandibular first molar model was preferred for the experimental tests and numerical study, as it represents the type of tooth most commonly subjected to endodontic therapy and additionally the model that presented the critical curvature of the two. The point of maximum curvature (smallest radius of curvature r = 2.81 mm) in the tertiary curvature, *Figure 2.10* with approximately *2* mm of instrument's tip exiting the root canal was at 0.43 mm from the apex .

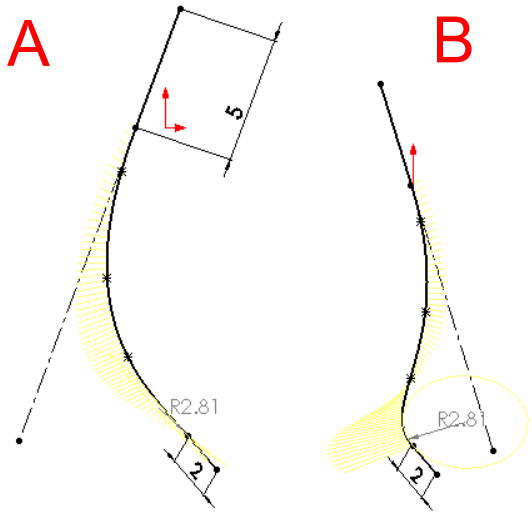

Figure 2.10 - Mandibular first molar root canal spline front view (bucolingual) (A) and right view (mesiodistal) (B).

Figure 2.11 - Front view (A) of the stainless steel mandibular first molar .

3. Numerical simulation

The numerical study was executed to approximately assess the *Hyflex™ CM* 20/04 file (Figure 3.1) mechanical response when subjected to the mandibular first molar root canal multi curvature. Due to the occurrence of large file deformation and the non-linear characteristic of Nitinol, a non-linear finite element analysis *FEA* was conducted through the *Solidworks™ FEA* package *Solidworks Simulation,* formerly known as *COSMOSworks.* Firstly, it was modelled a simplified instrument *CAD* model without flutes, using *Solidworks™* (Figure 3.2). The material characteristics were formulated for the analysis and the displacements were imposed to the model in order to simulate the curvature imposed by the root canal, finally the finite elements mesh was created and the simulation was executed.

3.1 Instrument CAD model.

HyFlex™ CM NiTi files geometry can be defined by three distinct areas, A, A-1 and B (shown in the *Figure 3.1*). (A-1) is the most important area of the file as it is responsible for shaping the root canal with a specific taper angle and diameter. The characteristic fluted geometry of this area is achieved by grinding a NiTi CM wire to a desired tip diameter and taper angle. The non-ground NiTi area (A) of the file improves the work range of the instrument along the root canal while the area depicted as (B) is attached to a slow speed micro motor handpiece.

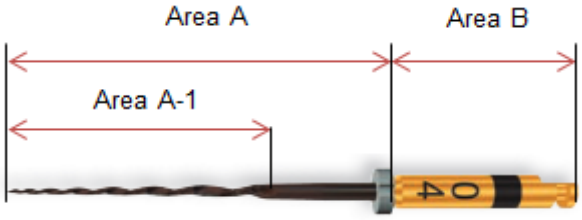

Figure 3.1 - *HyFlex™ CM* file with the different areas specified.

The current study focus on a *Hyflex™ CM* 20/04 instrument, and 20/04 is the reference for the tip diameter of 0.20 mm and the taper of 4%, additionally the diameter of the non-tapered region is 0.84 mm The respective length of the (A), (A-1) and (B) areas are 25 mm, 16 mm and 12.5 mm. The simplified instrument geometries with and without the fluted area are shown in the *Figure 3.2* and *Figure 3.3,* respectively.

Figure 3.2 - Simplified *Hyflex™ CM* 20/04 CAD model.

Figure 3.3 - Simplified fluted *Hyflex™ CM* 20/04 CAD model.

3.2 Material formulation

The material properties considered for the non-linear analysis are specified in the *Figure 3.4* and reflect the approximate stress-strain response, during loading and unloading stages of a typical control memory Nitinol wire used for fabrication of endodontic instruments, *Figure 1.14* D 48CM wire with 1.22 mm of diameter . An approximation for the initial and final yield stresses for both tensile and compressive loading/unloading stages were required for the simulation software as it didn't accept the introduction of null or zero values. The elastic modulus was considered with an approximated value of 43 GPa, respectively lower than an austenite based wire and higher than a fully martensitic wire. The maximum elongation was specified as 15% (Figure 3.5).

Property	Value
Poisson's Ratio	0.3
Initial Yield Stress (Tensile Loading)	190
Final Yield Stress (Tensile Loading)	240
Initial Yield Stress (Tensile Unloading)	10
Final Yield Stress (Tensile Unloading)	5
Initial Yield Stress (Compressive Loading)	190
Final Yield Stress (Compressive Loading)	240
Initial Yield Stress (Compressive Unloading)	10
Final Yield Stress (Compressive Unloading)	5
Ultimate Plastic Strain Measure (Tension)	0.15

Figure 3.4 - *Solidworks Simulation* Nitinol properties specification, (stress values are in MPa)

3.3 Displacement definition

To simulate the *Hyflex™ CM* 20/04 deformation within the mandibular first molar model and with 2 mm of tip exiting the root canal, it was imposed three-dimensional translations to 18 points, distancing 0.325 mm, along the simplified endodontic file active surface area (A-1), *Figure 3.2.* The mechanism for measuring the translations along the X, Y, and Z local axis is shown in the *Figure 3.5* and the specific results are in the *Table 3.1*.

The top cylindrical surface and top surface (area B) were considered fixed in the study as it is the attachment zone for the micro motor handpiece. The maximum displacement along the X and Z axis was respectively 7.18 mm and 3.63 mm.

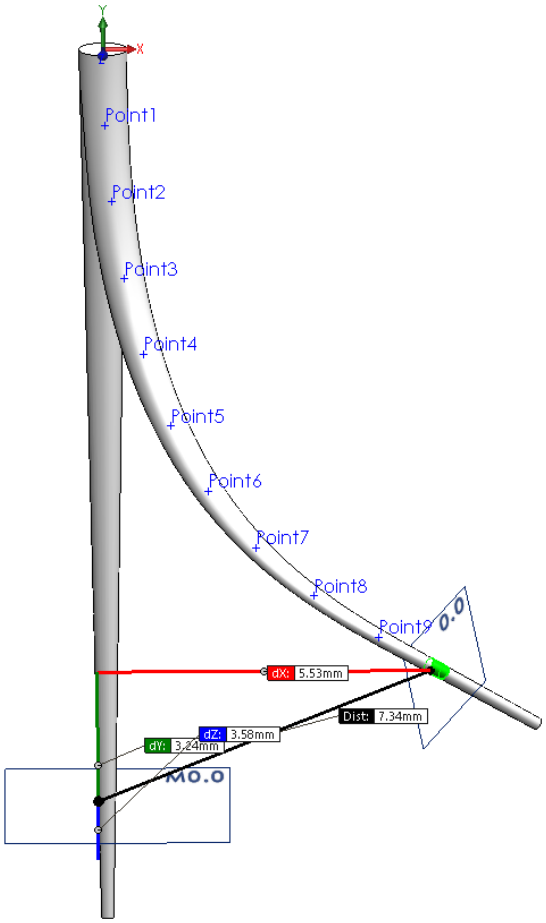

Figure 3.5 – Distance between corresponding points of the same original undeformed and posterior deformed instrument along the X, Y and Z local axis.

Table 3.1 - Three dimensional translations imposed to the points along the active surface area (A-1) used for the numerical analysis, the values in bold are correspondent to the valuesspecified for the Reference Geometry-23.

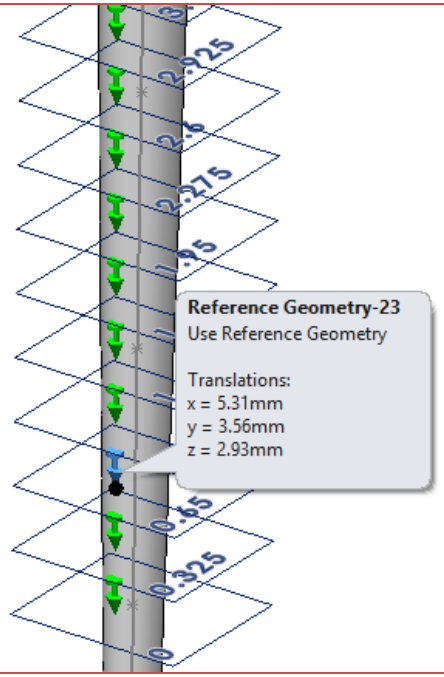

Point	Distance from the file tip in (mm)	Translation value along the X axis in (mm)	Translation value along the Y axis in (mm)	Translation value along the Z axis in (mm)
1	2	5.82	3.4	3.24
2	2.325	5.58	3.49	3.08
3	**2.65**	**5.31**	**3.56**	**2.93**
4	2.975	5.03	3.59	2.77
5	3.3	4.75	3.59	2.61
6	3.625	4.48	3.55	2.44
7	3.95	4.2	3.49	2.27
8	4.275	3.92	3.41	2.1
9	4.6	3.65	3.32	1.93
10	4.925	3.38	3.21	1.76
11	5.25	3.12	3.09	1.59
12	5.575	2.86	2.96	1.41
15	6.55	2.16	2.48	0.93
16	6.875	1.96	2.3	0.79
17	7.2	1.77	2.12	0.67
18	7.525	1.59	1.95	0.55

3.4 Non-linear analysis

All the non-linear analysis were carried out using the direct sparse solver, with the incremental load control method and the Newton-Raphson iterative solution method; the loads in this case are the imposed displacements, which are incrementally applied as specified by the associated load curves. Both solver and the iterative solution method were preferred among others due to their higher chance of convergence when dealing with highly nonlinear problems.

In a first approach, two non-linear analyses were performed using a simplified instrument without the fluted area and with a lesser quality mesh constituted of first order elements. For the first analysis (1 – I) the prescribed displacements which are present in the *Table 3.1* represent the curvature of the instrument during the initial position with the initial 2 mm of tip exiting the root canal. The second analysis (1 – F) was performed with an identical mesh as the first one but with the prescribed displacements representing the instrument's deformation during the 3 mm higher position.

A mesh convergence study was carried out for the simplified instrument with lesser quality mesh to ensure that the non-linear analysis results were not affected by the variation of the mesh size. The maximum *Von Mises Stress* was plotted against the number of first order elements present in the mesh for six convergence runs *Figure 3.6*, the result shows that exists convergence of the non-linear analysis results.

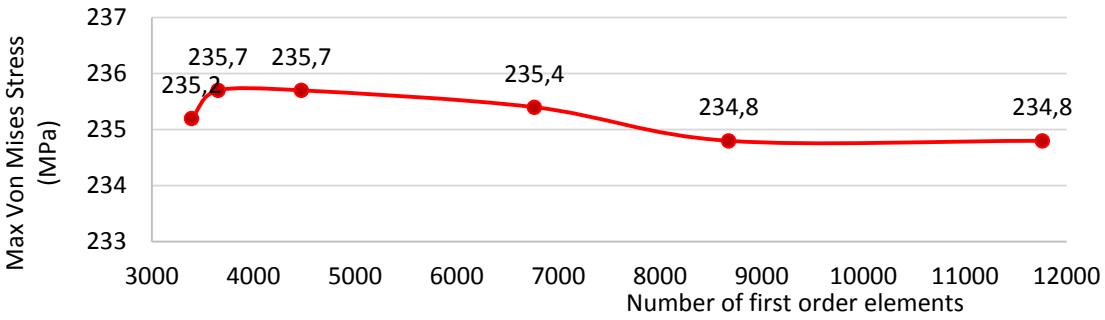

Figure 3.6 - Mesh convergence graph.

The second approach (2 - I) of the study was performed with the aim of assessing the results variation in relation to the type of element used, for this a single non-linear analysis was realized for the simplified instrument without flutes and with second order constituted mesh while making an approximation of the first approach initial position curvature.

The third approach (3 – I) assesses the importance of the fluted area on the simulation results, the simulation parameters, such as imposed displacements and mesh quality are similar to the parameters of the second approach. All the non-linear analysis initial results are shown for the three approaches, through the following figures from the *Figure 3.7* to *Figure 3.19,* in the Chapter 5 are present the exhaustive list of results.

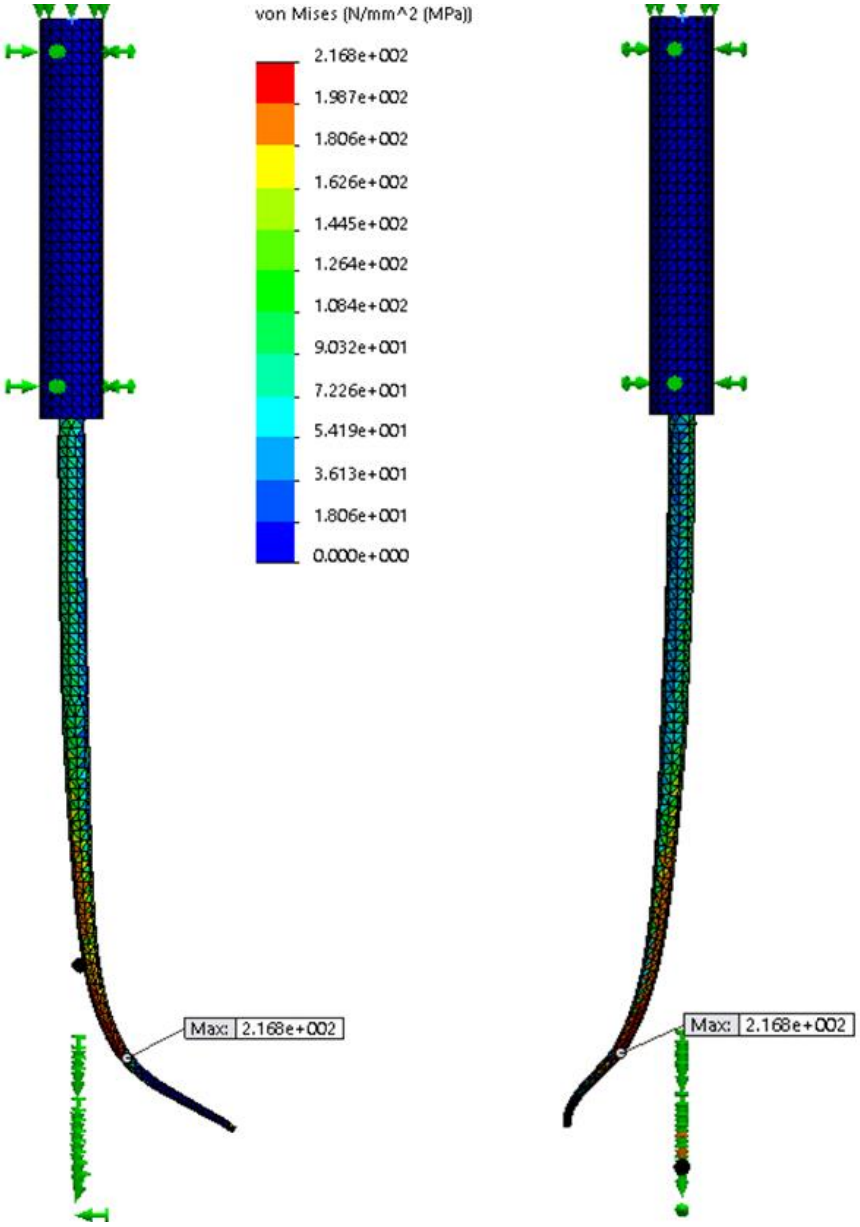

Figure 3.7 - Front and left view of the equivalent Von mises stress distribution along the simplified geometry in the top position.

Table 3.2 - Mesh details for the simplified geometry in the top position (1 – F).

(1 – F) Mesh Details	
Mesh type	Solid mesh
Mesher Used	Standard mesh
Elements type	First order
Maximum element size	0.35 mm
Total elements	8527
Percentage of elements with Aspect ratio >10	0

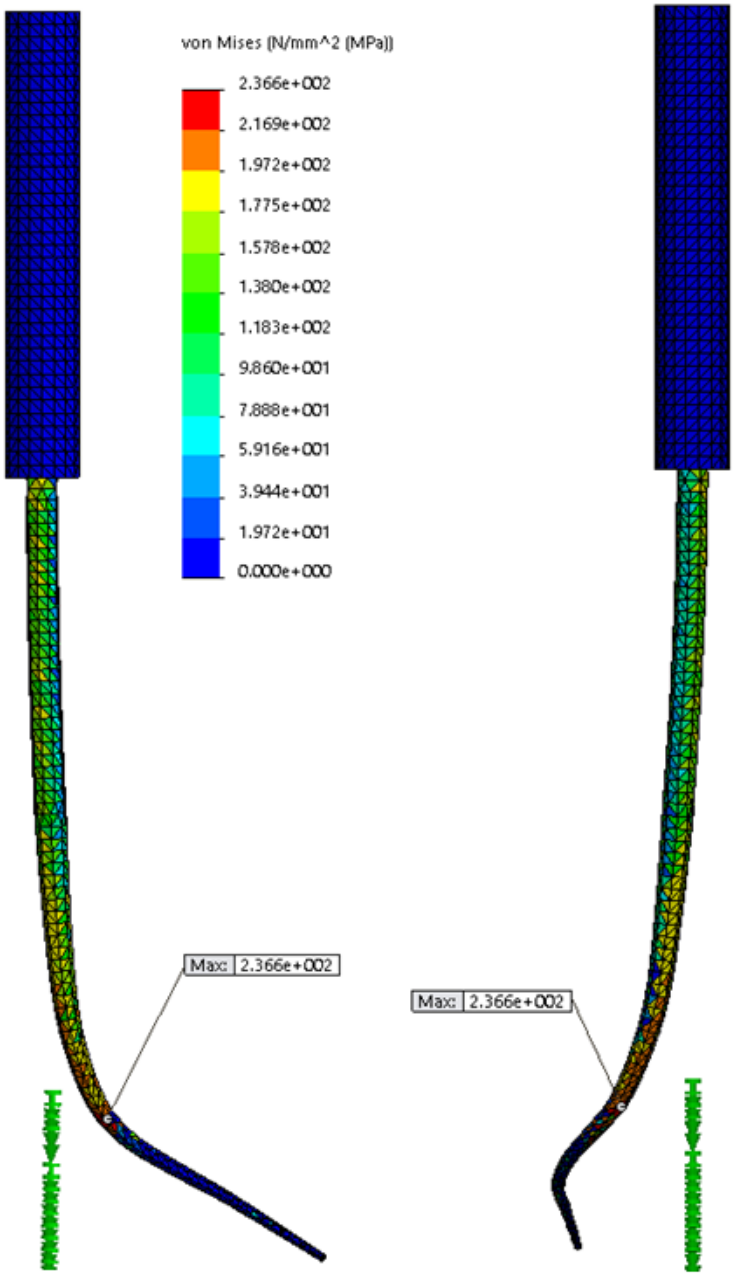

Figure 3.8 - Front and left view of the equivalent Von mises stress distribution along the simplified geometry in the initial position (1 - I)

Table 3.3 - Mesh details for the simplified geometry in the initial position.

(1 – I) Mesh Details	
Mesh type	Solid mesh
Mesher Used	Standard mesh
Elements type	First order
Maximum element size	0.35 mm
Total elements	8684
Percentage of elements with Aspect ratio >10	0

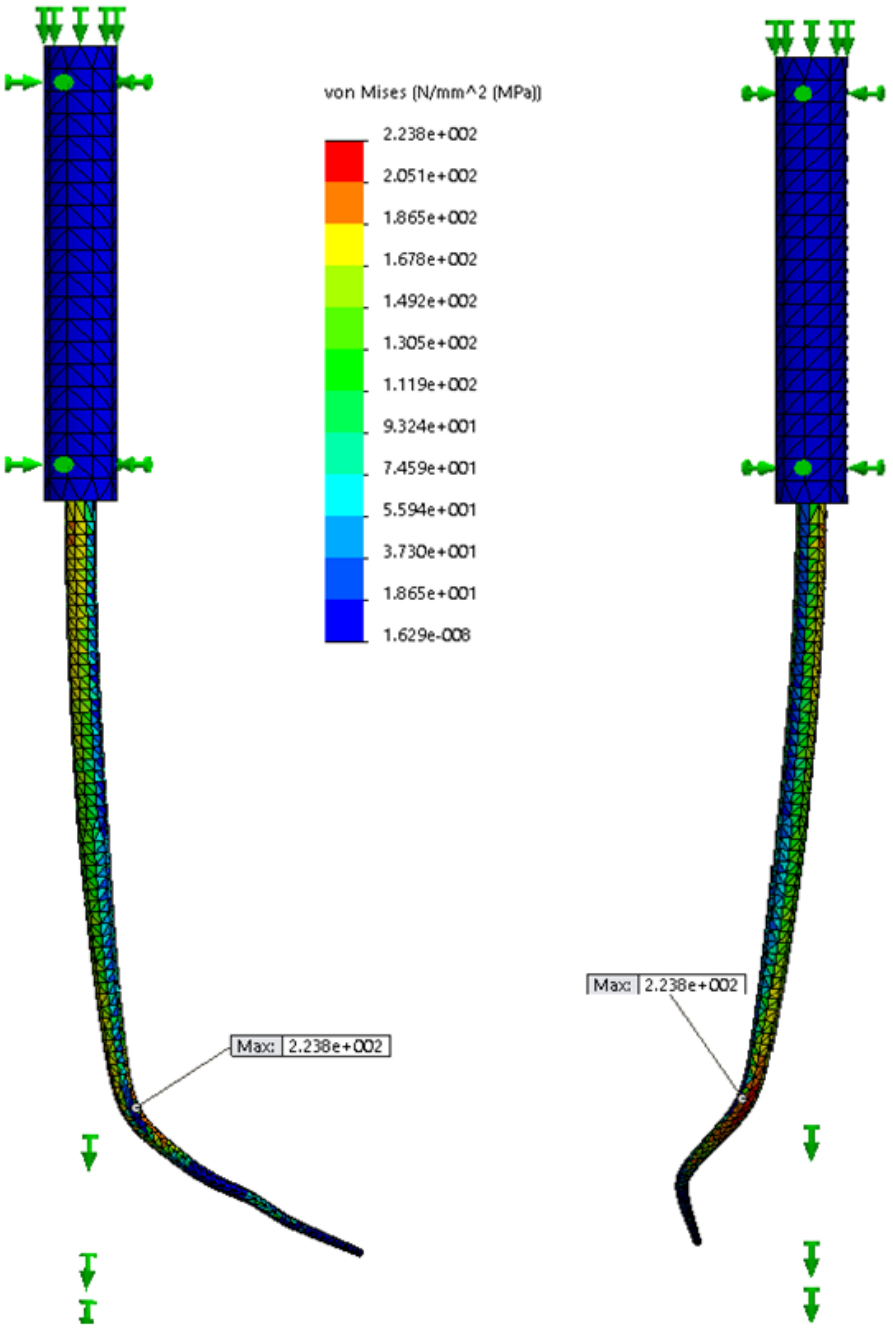

Figure 3.9 - Front and left view of the equivalent Von mises stress distribution along the simplified geometry in the initial position with higher quality mesh (2 – I)

Table 3.4 - Mesh details for the simplified geometry in the initial position.

(2 – I) Mesh Details	
Mesh type	Solid mesh
Mesher Used	Standard mesh
Elements type	Second order
Maximum element size	0.65 mm
Total elements	3421
Percentage of elements with Aspect ratio >10	0.029

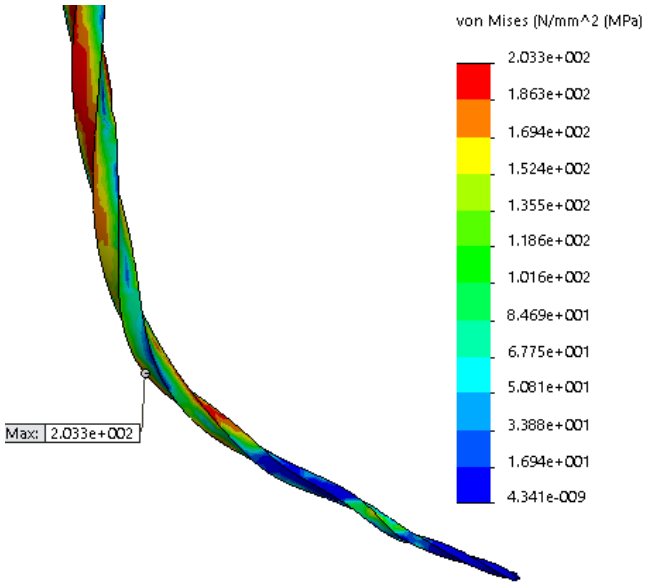

Figure 3.10 - Front view of the equivalent Von mises stress distribution along the fluted simplified geometry in the initial position with higher quality meh (3 – I).

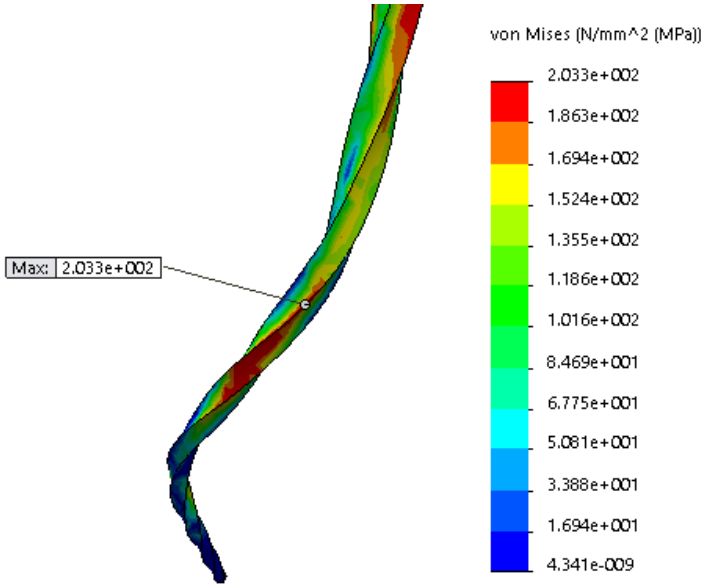

Figure 3.11 - Left view of the equivalent Von mises stress distribution along the fluted simplified geometry in the initial position with higher quality mesh (3 – I).

Table 3.5 - Mesh details of the fluted model in the intial position.

(3 – I) Mesh Details	
Mesh type	Solid mesh
Mesher Used	Standard mesh
Elements type	Second order
Maximum element size	0.72 mm
Total elements	2934
Percentage of elements with aspect ratio >10	0.136

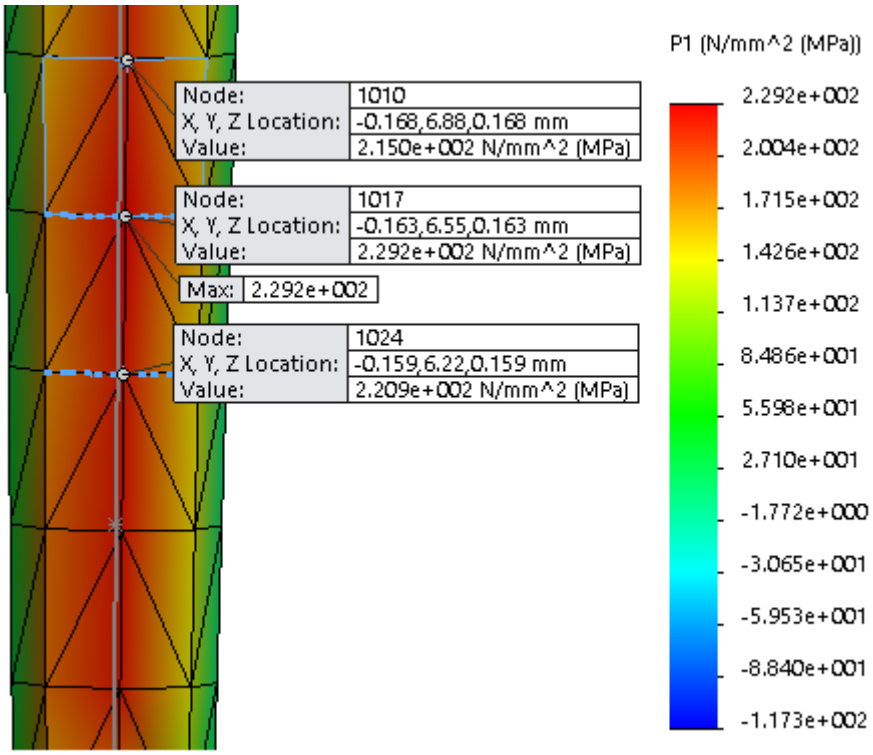

Figure 3.12 - First principal stress (P1) distribution along the simplified model with lower quality mesh in the top position (1 – F).

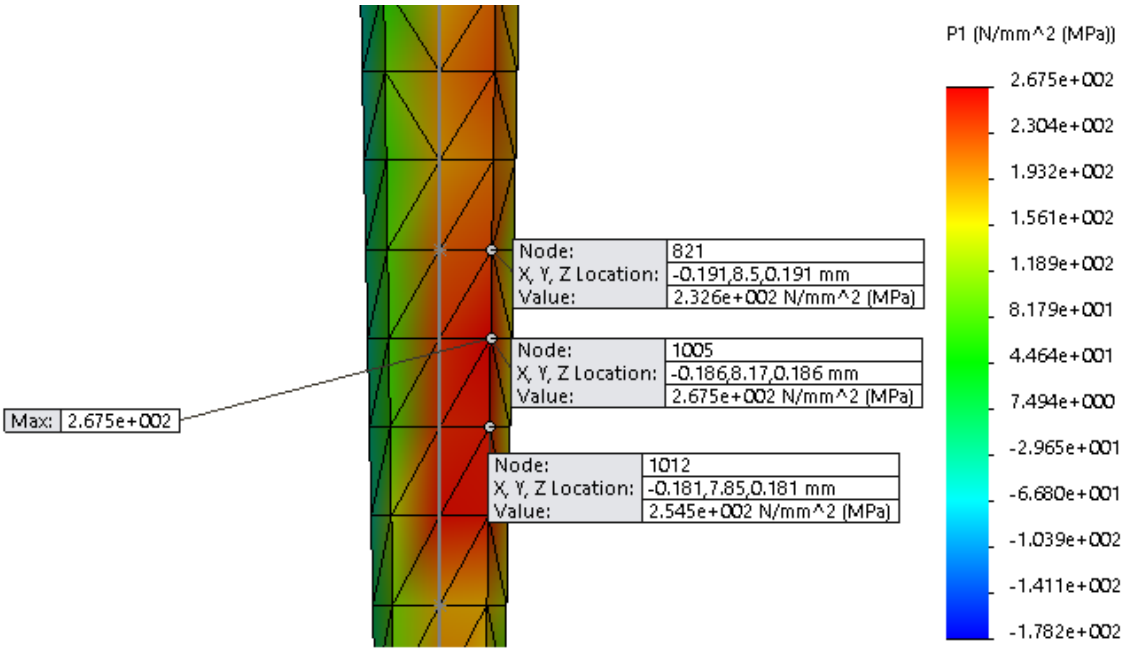

Figure 3.13 - First principal stress (P1) distribution along the simplified model with lower quality mesh in the initial position (1 – I).

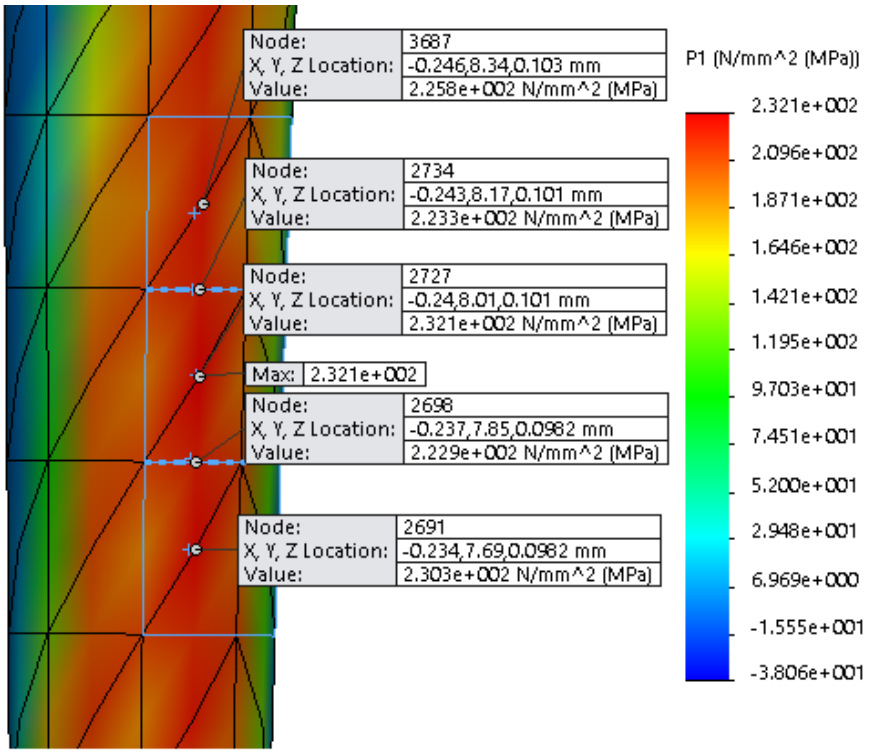

Figure 3.14 - Nodal first principal stress(P1) distribution for the simplified model with high quality mesh in the initial position (2 – I).

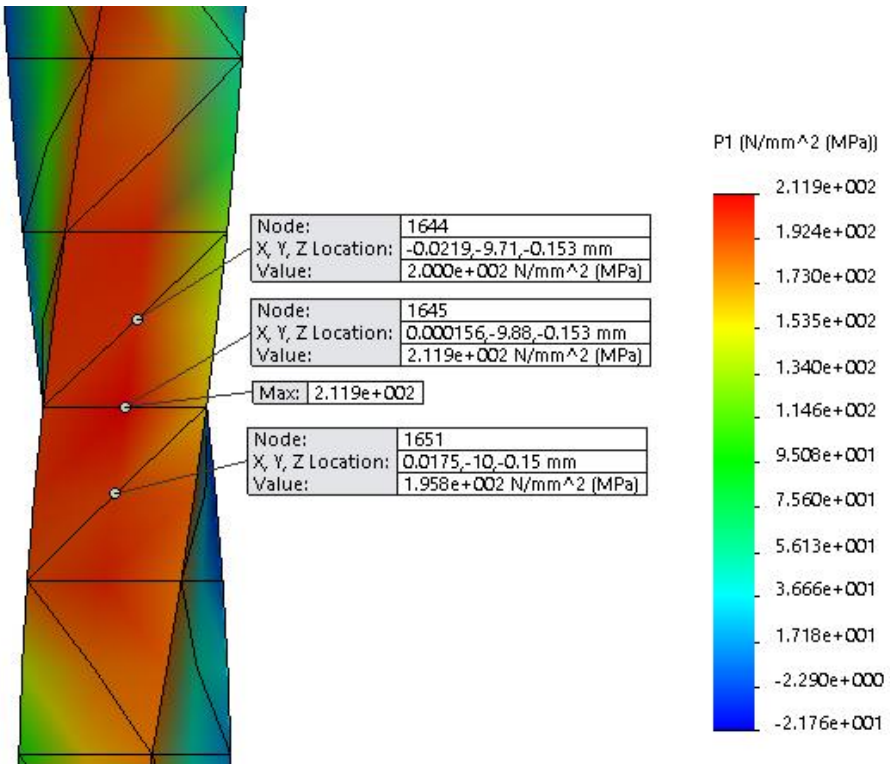

Figure 3.15 - Nodal first principal stress (P1) distribution along the fluted model with high quality mesh in the initial position (3 – I).

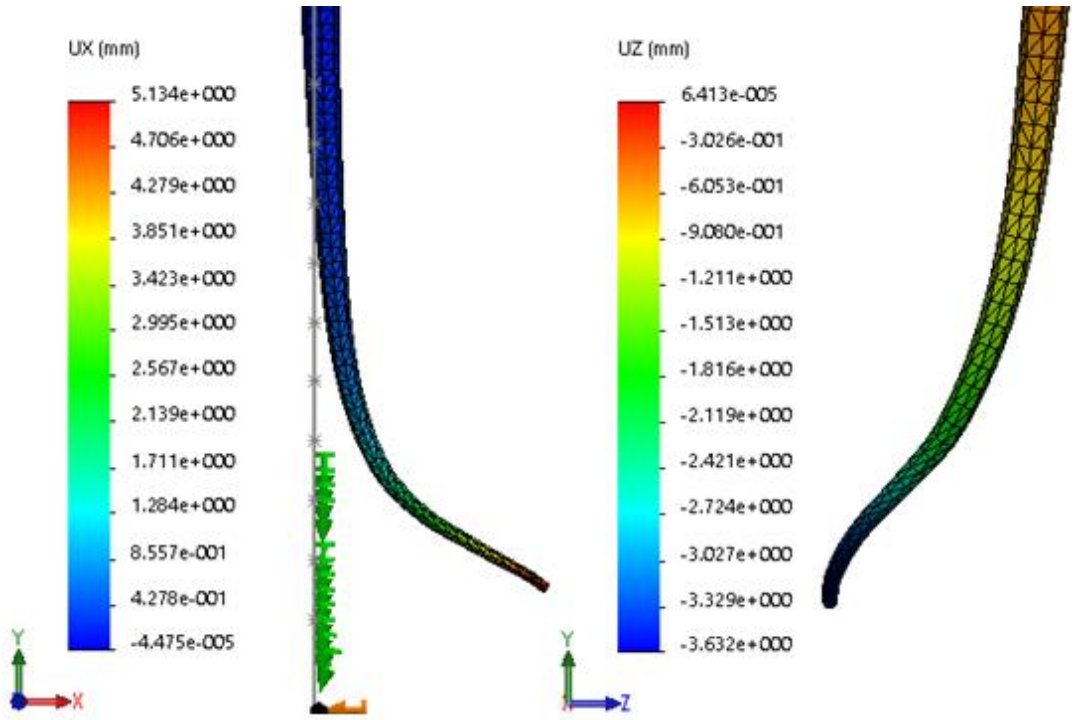

Figure 3.16 - Resultant maximum *X* and *Z* local displacements on the (1 – F) analysis.

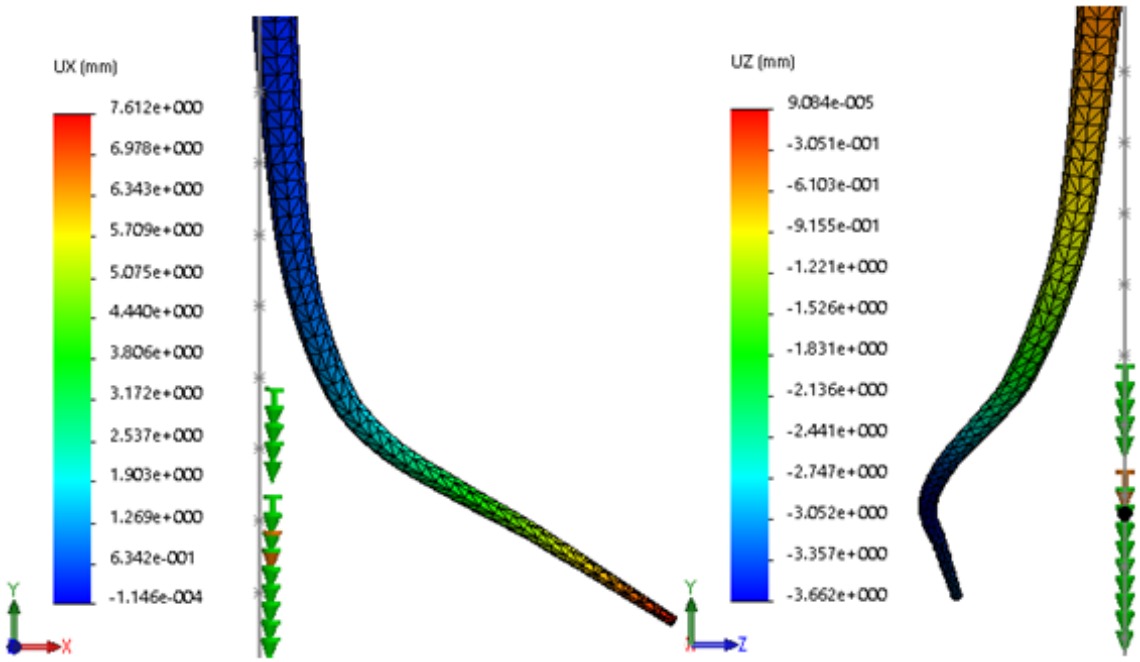

Figure 3.17 – Resultant maximum *X* and *Z* local displacements on the (1 – I) analysis.

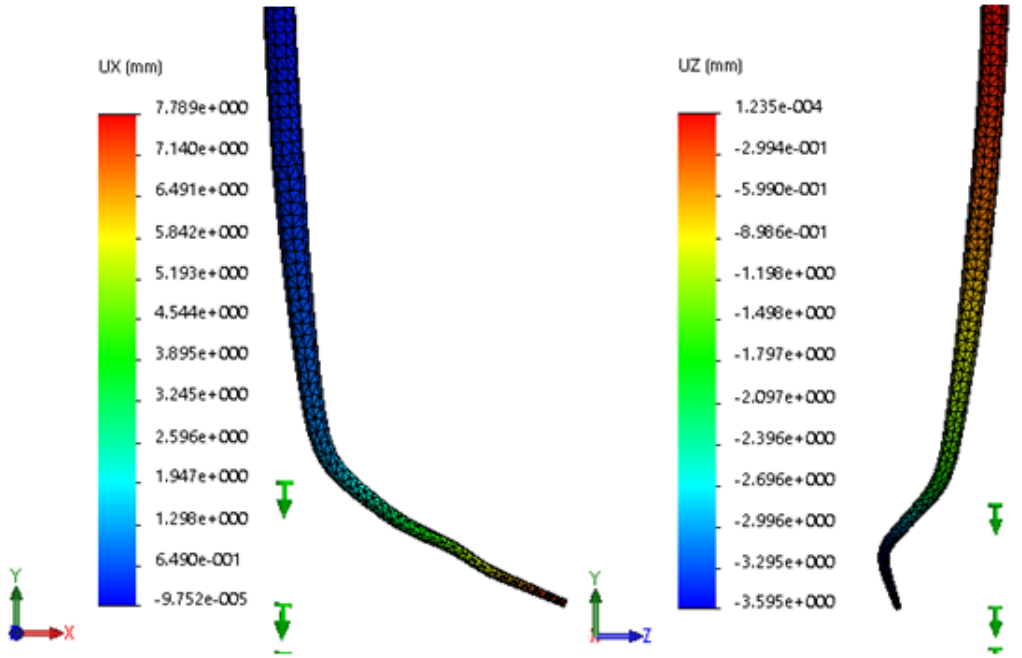

Figure 3.18 - Resultant maximum *X and Z* local displacements on the (2 – I) analysis.

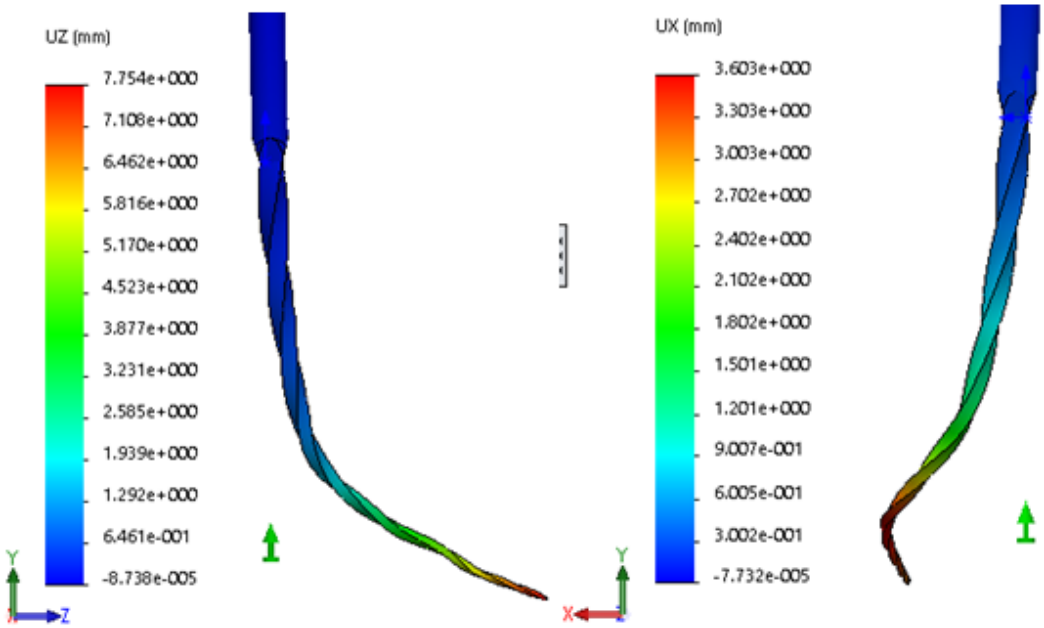

Figure 3.19 - Resultant maximum *Z* and *X* local displacements on the (3 – I) analysis.

4. Experimental setup

In this chapter, the design considerations concerning the experimental setup for the evaluation of dynamic cyclic fatigue have been explained.

The system was designed in order to replicate the relative movement between tooth and the endodontic instrument as would occur during a real treatment procedure. The relative movement can be decomposed in two independent relative movements, the axial movement, simulating pecking motion and the rotational movement provided by a handpiece. Such movements have been created by two independent mechanisms, the axial motion and the rotational motion mechanisms. In order two assess and compare the instrument's fatigue life two types of tests were conducted; Axial static tests, using the rotational motion mechanism to simulate typical rotational cycles. Dynamic tests, using both motion mechanisms to recreate typical rotational cycles with pecking motion.

4.1 Axial motion mechanism

The iterative process of designing the axial motion mechanism had in consideration the single functional requirement of providing axial motion to a tooth in the vertical direction and several constraints, such as being a simple cost-effective design solution and at same time reliable with the possibility to accommodate future modifications and extensions. It also needed to grant the dynamic and axial static cyclic fatigue life tests replicability.

The final design solution for the axial motion mechanism *Figure 4.1* consists in using a stepper motor driven linear table to move a specifically created part by which is possible to fix the tooth model.

Figure 4.1 - Solidworks™ final design solution assembly of the axial motion mechanism.

4.1.1 Linear table

Considering that maximum load and maximum movement distance wasn't a constraint, it was chosen a drylin ® SHTP-01-06-AWM linear table with 100 mm of displacement *Figure 4.2* and characterized by its corrosion resistance due to having carriages and shaft end supports made of high performance polymers, as well as an aluminium lead screw. The adoption of the lead screw in a vertical position permitted the annulment of the *backlash* effect on the movement; this is the error in the positioning of the carriage in relation to the leadscrew due the gap between threads of the nut and leadscrew therefore maintaining the replicability of the movement.

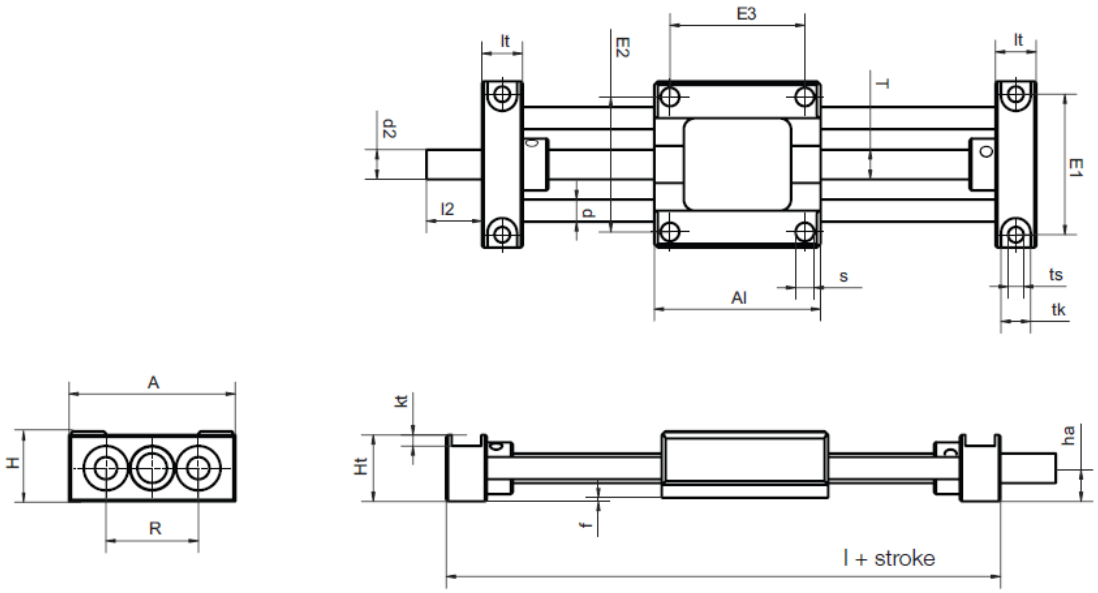

Figure 4.2 - Technical drawing of the drylin SHTP-01-06-AWM linear table.

4.1.2 3D printed components

The tooth model support, linear table fixation supports and the hand piece fixation supports were printed in *BQ™ Prusa I3* 3D printer using a PLA filament with specific characteristics see *Table 4.2*. PLA (Poly-Lactic Acid) is a thermoplastic which is extruded from starch plants such sugarcane and corn. The printing specifications are shown in the following table.

Table 4.1 - *BQ Prusa™ I3* 3D Printer, printing specifications.

Printing specifications	
Precision	Layers of 0.1 mm
Extrusion head diameter	0.4 mm
Printing temperature	250 ± 5ºC

Table 4.2 – 3D printer filament specifications

Filament specifications	
Material	PLA
Transparency	Opaque
Diameter	1.75 mm
Diametral tolerance	+ 0.1 mm / - 0.15 mm
Ovality tolerance	± 5%
Specific mass	1250 kg/m^3
Melting temperature	180 to 200 ºC
Impact strength	5 Kj/m^2

4.1.3 Stepper motor

To maintain the replicability of every experimental procedure, a stepper motor as chosen to power the axial movement mechanism, as this type of motors are characterized by the ability of achieving very precise motion . Stepper motors have multiple coils arranged in groups called phases, which are turned on and off by a control system to make the motor shaft move in discrete steps. By activating each coil in a specific order it is possible to drive the motor shaft one step at a time or turn 1.8 degrees at a time if it's a 1.8 Deg. /Step stepper motor.

Table 4.3 - Stepper motor characteristics.

NEMA 17	
Drive method	Bi-polar
Number of phases	2
Step angle	Deg./Step 1.8
Voltage	12 V
Current	0.35 A per phase
Holding torque	200 mN.m

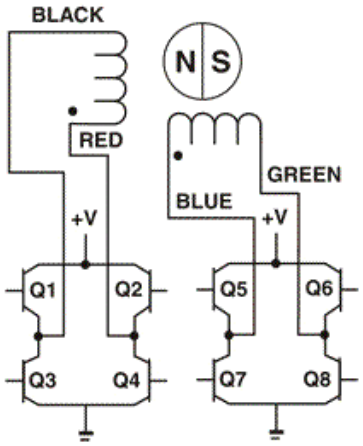

Figure 4.3 - Bipolar stepper motor winding arrangement.

4.1.4 Aluminium flex shaft coupler

To connect the linear table to the stepper motor, it was chosen a set-screw coupler made of a machined aluminium cylinder with a spiral cut that makes it slightly flexible. The increased flexibility helps coupling two shafts with a slight deviation from perfect collinearity.
The coupler is flexible in the X Y and Z linear axis; although it will not decrease the precision of the rotation movement as it's not flexible in the rotational axis and will not increase the backlash effect.

Table 4.4 Aluminium flex shaft coupler technical specificantions

Coupling shafts diameter (mm)	Diameter (mm)	Height (mm)	Weight (grams)
5 to 8	18	25	15

4.2 Rotational motion mechanism

The rotational motion was provided to the endodontic instrument by a *Wave One Primary*™ micro motor hand piece, which is rotation speed and torque configurable.

4.3 Axial motion control system

The axial motion control system, consisting of a control and power circuits with specific software, controls the linear table movement speed and distance travelled during experiments by setting the stepper motor rotation speed and number of steps to be concluded. The control and power circuits were created by attaching an *Adafruit motor shield v2.0* ™ to an *Arduino*™ *Uno* microcontroller board. This specific configuration improved the extensibility of the project, as it is able to control up to 4 DC motors or 2 stepper motors.

The experimental tests were conducted through a specific created VBA control panel *Figure 4.4*.

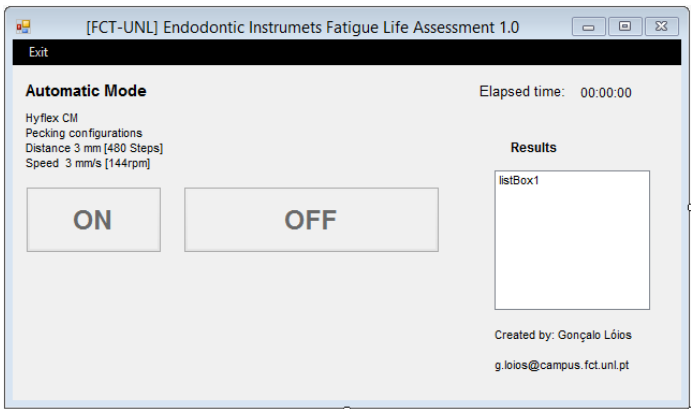

Figure 4.4 - Experimental fatigue life assessment control panel.

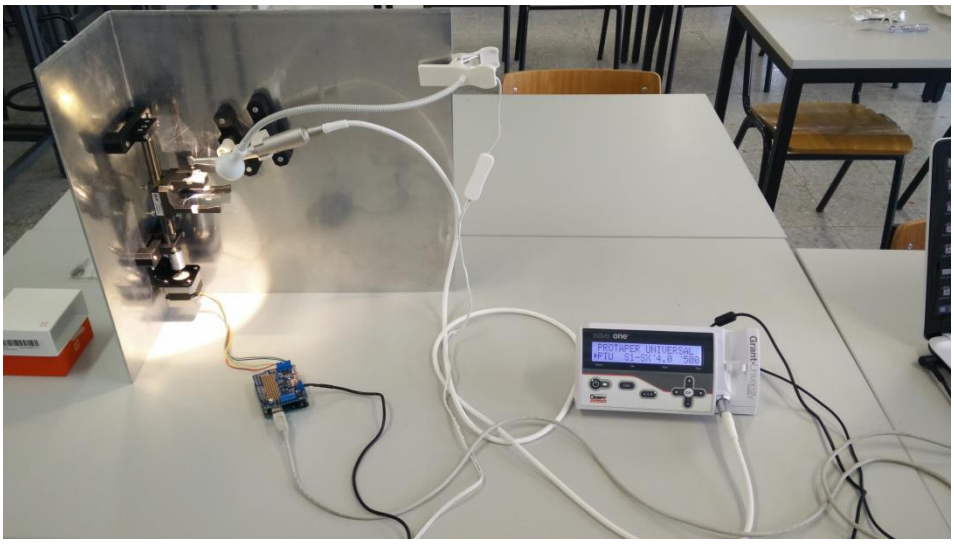

Figure 4.5 - Experimental setup.

4.4 Testing procedure

1- Install the endodontic instrument in the micro motor by rotating until it achieves a fixed position.

2- Certify that there is no holding torque in the stepper motor. Remove the holding torque by disconnecting the stepper motor from the power source.

3- Manually move the support base to the starting postion, where is possible to have 2 mm of intrument tip exiting the root canal, see *Figure 4.6*.

4- Connect the stepper motor and the WaveOne micromotor to the power source.

5- Set the recommended rotation speed of 500 rotations per minute for the *Hyflex™ CM* instruments in the WaveOne controler.

6- (Dynamic test) Press the WaveOne pedal switch and the ON button on the control panel at the same for start testing. (Axial static test) Press only the WaveOne pedal switch, use a chronometer to record the time until instrument fracture. Note the WaveOne pedal switch must be kept pressed during testing see *Figure 4.5*.

7- (Dynamic test) Press the OFF button on the control panel and release the pedal switch as soon as the fracture happens on the endodontic instrument.

8- Recover the fractured instrument's tip.

9- Remove the holding torque from the stepper motor and manually move the support base down to obtain clearance with the aim of removing the instrument from the micro motor.

10- Repeat the procedure for the remaining instruments.

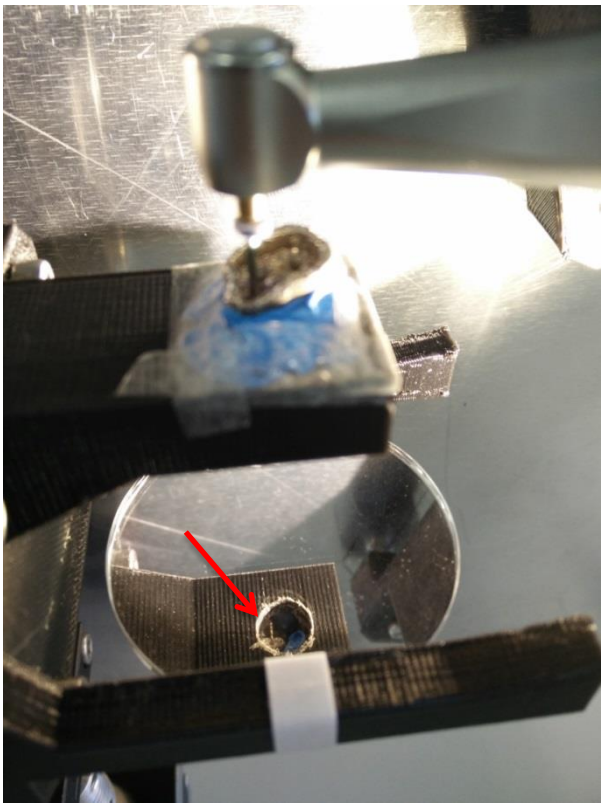

Figure 4.6 - *Hyflex™ CM* starting relative position, the red arrow indicates the aproximate 2 *mm* of instrument tip exiting the root canal in the apical region.

5. Results

5.1 Non-linear finite element analysis results

The maximum values for the equivalent Von Mises stress results for all the analyses are shown on the *Table 5.1.* They are all located on the secondary curvature of the root canal and present values lower than the maximum yield stress of material (240 MPa).

Table 5.1 - Maximum values calculated for the equivalent Von Mises Stresses (MPa) and respective location. Results obtained through non-linear analysis.

Non-linear analysis	Maximum Von Mises Stress (MPa)	Double curvature positioning
(1 – F)	216.8	Secondary
(1 – I)	236.6	Secondary
(2 – I)	223.8	Secondary
(3 – I)	203.3	Secondary

The maximum first principal stress results with the respective location of fracture occurrence in the instrument's length are shown, for each analysis, on the *Table 5.2*. The analysis (1-F), (1-I) and (3-I) displayed stress values lower than the maximum yield stress of 240 MPa, while the analysis (1-I) displayed a stress value higher than 240 MPa. All the maximum first principal stress occurred on the secondary curvature of the root canal.

Table 5.2 - Maximum first principal stress P1 with the respective location results and respective distance from the instrument's tip.

Non-linear analysis	Maximum first principal stress P1 (MPa)	Distance from maximum P1 location to instrument tip (mm)	Double curvature positioning
(1 – F)	229.2	6.55	Secondary
(1 – I)	267.5	8.17	Secondary
(2 – I)	232.1	8.01	Secondary
(3 – I)	211.9	6.12	Secondary

The maximum tip displacement resulted from the non-linear analysis, along the X and Z directions in the *Table 5.3* are comparable to the original root canal path maximum distance from the origin, in fact the relative error between the two is inferior to 10%.

Table 5.3 - X and Z maximum non-linear analysis displacemets with the relative error.

Non-linear analysis	*X* maximum displacement (mm)	*Z* maximum displacement (mm)	X relative error (%)	Y relative error (%)
(1 – F)	5.134	3.632	-	-
(1 – I)	7.612	3.662	6.01	3.2
(2 – I)	7.789	3.595	8.48	3.5
(3 – I)	7.754	3.603	7.99	2.7

5.2 Experimental results

In a total of 12 tested instruments, 3 were subjected to the axial static test and 9 were subjected to the dynamic test, forming the groups A and B, respectively.

Both groups had their time to rupture recorded, which is presented in *Table 5.4*. The measured fractured segments lengths are shown in *Table 5.5.*

Table 5.4 – Axial static (A) and Dynamic (B) experimental test results.

Group	Instrument	Rupture region	Test duration [seconds]	Average test duration [seconds]	Standard deviation [seconds]
A	.04/20_1	Coronal*	70	-	-
	.04/20_11	Apical	131	119	12
	.04/20_12	Apical	107		
B	.04/20_2	Apical	177	194.1	53.9
	.04/20_3	Apical	255		
	.04/20_4	Apical	248		
	.04/20_5	Apical	114		
	.04/20_6	Apical	110		
	.04/20_7	Apical	244		
	.04/20_8	Apical	155		
	.04/20_9	Apical	212		
	.04/20_10	Apical	232		

Table 5.5 – Axial static (A) and Dynamic (B) experimental test results.

Group	Instrument	Rupture region	Fractured segment length [mm]	Average fractured segment length [mm]	Standard deviation [mm]
A	.04/20_1	Coronal*	13.0	-	-
	.04/20_11	Apical	4.30	4.90	0.6
	.04/20_12	Apical	5.50		
B	.04/20_2	Apical	3.30	4.13	0.33
	.04/20_3	Apical	4.30		
	.04/20_4	Apical	4.10		
	.04/20_5	Apical	4.45		
	.04/20_6	Apical	4.05		
	.04/20_7	Apical	4,50		
	.04/20_8	Apical	4,20		
	.04/20_9	Apical	4,30		
	.04/20_10	Apical	4,0		

6. Results discussion

It's known from the *Chapter 1.7* that mode-I fatigue crack propagation occurs when fracture surface is perpendicular to the maximum principal stress P1 applied, that is when subjected to predominant cyclical loads of pure bending without any evidence of torsional loads. Considering the endodontic instruments tested, that followed curved paths, the resulting maximum P1 stresses are due to the combination of different factors, for example the existence of large curvatures along the root path (smaller radius of curvature), with large instrument cross section, or distance to instrument's axis or the existence of stress concentration factors, such as material defects, small notches introduced during grinding and the flute geometry, just to mention few.

Considering experimental data, the fracture surface at instrument's tip always displayed perpendicular alignment to the respective instrument's axis, suggesting that crack propagation occurred due to mode-I type (Annex K).

From the twelve instruments tested, a group of three instruments (group A), namely the .04/20_1, .04/20_11 and .04/20_12 instruments, were subjected to "axial static" test (without *Pecking Motion).* However, the .04/20_1 instrument was discarded from the final results due to fracture occurrence in the coronal region resulting from bad alignment with the tooth model's root entrance, causing premature rupture. Nevertheless, it proved that instruments tested are not suitable to work in such a region of tooth.

The group B was constituted by nine instruments subjected to the dynamic test (rotational bending and pecking motion), and displayed an average test duration of extra 75.1 seconds than mean duration verified of instruments belonging to group A *Table 5.4*, even considering scatter. This difference suggests that the application of the so called *Pecking Motion* had beneficial influence on the instruments fatigue life. The fractured tip's length measurements carried out from both groups are also in accordance with this idea, as group B average fractured tip's length was 0.77 mm smaller than of the group A average. This difference can be explained by the dislocation over time of the maximum first principal stress location when there is relative motion along the root canal path between instrument and the maxillary first molar model with multi planar curvatures.

Considering the non-linear finite element analysis carried out, the instrument's deformation (model) replicated the real instrument deformation when inserted in the maxillary first molar root canal path with multi planar curvature *Figure 2.9* and *Figure 3.10,* both displaying similar primary, secondary and tertiary curvatures.

The numerical analysis and the experimental tests displayed similar results for the location where fracture occurred; however, any small discrepancies can be justified by the non-existence of stress concentration factors in the numerical analysis, the error related to the exact positioning of the instrument inside the mandibular first molar numerical model and small

imprecisions related to the location of the imposed translations in the non-linear numerical analysis.

The maximum P1 value is lower than the maximum yield stress of 240 MPa for the (3 – I) non-linear analysis, which has the modelled geometry that better describes the geometry of the real instrument, although rupture by fatigue can still occur due to the presence of fatigue stress concentration factors. For this analysis, the predicted location for the occurrence of the fracture is 6.12 mm away from the instrument's tip and is comparable to the experimental results from the group A, as it represented the same initial condition of 2 mm of instrument's tip exiting the root canal; therefore, this suggests good convergence between experimental and numerical results when there is a closer replication of the instrument and also of the instrument position in the non-linear analysis.

Finally, it's important to note that instruments fractured in a location corresponding to the root canal's secondary curvature and not in the tertiary curvature, where instruments display the smallest radius of curvature ($r = 2.81$ mm). This suggests that the larger instrument's cross section at this specific location (secondary curvature) had an important effect in its total fatigue life.

7. Final conclusions and proposals of future Work

Twelve *Hyflex™ CM* 20/04 instruments were tested using an experimental setup specially designed to simulate the rotational and vertical relative movements usually found on a typical endodontic therapy procedure and which are responsible for the instruments fracture by fatigue failure. A mandibular first molar model was used to replicate a real root canal with multiple curvatures, which were confirmed by radiography. Two experimental groups were formed, the A group constituted of three instruments subjected to only rotational movement and the B group constituted of nine instruments subjected to the combination of both type of movements (axial and bending). One instrument test result from group A was discarded due to the bad initial positioning on the testing system (it fractured in the coronal region);, the two remaining instruments from group A displayed an average time to fracture of 119 seconds and an average fractured tip length of 4.9 mm. The experimental results of the nine instruments from group B displayed an increased average time to fracture of 194.1 seconds and a smaller average fractured tip length of 4.13 mm.

Four non-linear FE analyses were carried out for two different instrument placement conditions, the top position representing analysis (1-F) shown a maximum equivalent first principal stress of 229.2 MPa and a fractured tip length of 6.55 mm. The best initial position representing analysis (3-1) shown a maximum equivalent first principal stress of 211,9 MPa and a fractured tip length of 6.12 mm.

Both numerical and experimental approaches displayed similar locations for the occurrence of fracture considering the same instrument placement, although they differ from the location of maximum curvature on the root canal path.

Modifications to the existent experimental setup and control code would need to be carried out, in order to adapt it to the realization of further experimental tests that would take into account the effect of temperature generated by friction during the experiment and the effect of the variation of vertical motion speed on the results.

8. References

[1] (5/3/2015). http://en.wikipedia.org/wiki/Endodontic_therapy.

[2] (15/3/2015). http://www.nature.com/bdj/journal/v197/n10/full/4811823a.html.

[3] (15/3/2015). http://www.med-college.hu/de/wiki/artikel.php?id=302&lan=2.

[4](15/3/2015). http://www.hyflexcm.com/DevDownloads/31031A_2014_EndoCatalog.pdf.

[5] Matthias J. Roggendorf, “Case report for the new HyFlex™ CM NiTi File system of Coltene Endo”

[6] Luca Testarelli; Gianluca Plotino; Dina Al-Sudani, et. al., “Bending Properties of a New Nickel-Titanium Alloy with a Lower Percent by Weight of Nickel”, *Journal of Endodontics* , vol. 37, no. 9, pp. 1293-5, September 2011.

[7] Georgia, B. Alexandrou; Konstantinos Chrissafis; Leonidas P. Vasiliadis; et. al., “Current Challenges and Concepts of the Thermomechanical Treatment of Nickel-Titanium Instruments” *Journal of Endodontics,* vol.39, no. 2,pp. 163-72, February 2013.

[8] Renata C.V. Rodrigues; Hélio P. Lopes; Carlos N.Elias; et. al., “Influence of Different Manufacturing Methods on the Cyclic Fatigue of Rotary Nickel-Titanium Endodontic Instruments”, *Journal of Endodontics*, vol. 37, no. 11,pp. 1553-7, November 2011.

[9] Thompson SA., “An overview of nickel–titanium alloys used in dentistry”, International Endodontic Journal, vol. 33, pp. 297-310, July 2000.

[10] Daniel Mutter; and Peter Nielaba, “Simulation of structural phase transitions in NiTi”, *Department of Physics, University of Konstanz*, vol. 82, no 22, December 2010.

[11] Alan R. Pelton; Scott M. Russel; and John DiCello, “The Physical Metallurgy of Nitinol for Medical Applications”, *Journal of Metals*, pp. 33-37, May 2003.

[12] T. Ezaz, H. Sehitoglu; and H.J Maier, “Energetics of twinning in martensitic NiTi”, Acta Materialia, vol. 59, no. 15, pp. 5893-5904, September 2011.

[13] E.Goo, T. Duerig; K. Melton; and R. Sinclair, “Mechanical Twinning in $Ti_{50}Ni_{47}Fe_3$ and $Ti_{49}Ni_{51}$ Alloys”, *Acta metall*, vol. 33, no. 9, pp. 1725-1733, November 1985.

[14] K.L. Ng; and Q.P. Sun, “Stress-induced phase transformation and detwinning in NiTi polycrystalline shape memory alloy tubes”, *Mechanics of Materials*, vol. 38, no. 1, pp. 41-56, January 2006.

[15] Hui-min Zhou; Ya Shen; Wei Zheng; Li Li; et al., “Mechanical Properties of Controlled Memory and Superelastic Nickel-Titanium Wires Used in the Manufacture of Rotary Endodontic Instruments”, *Journal of Endodontics*, vol. 38, no. 11, pp. 1535-1540, November 2012.

[16] Yinong Liu; and Hong Yang, “Strain dependence of the Clausius–Clapeyron relation for thermoelastic martensitic transformations in NiTi”, School of Mechanical Engineering, *University of Western Australia,* vol. 16, no. 1, pp. 22-27, January 2007.

[17] (04/04/2015) http://www.matweb.com.

[18] So-Ram Oh; Seok-Woo Chang; Yoon Lee; et. al., “A comparison of nickel-titanium rotary instruments manufactured using different methods and cross-sectional areas: ability to resist cyclic fatigue”, *Oral Surgery, Oral Medicine, Oral Pathology, Oral Radiology, and Endodontology,* vol. 109, no. 4, pp. 622-8, April 2010.

[19] Georgia B. Alexandrou; Konstantinos Chrissafis; Leonidas P. Vasiliadis; et. al,, “SEM Observations and Differential Scanning Calorimetric Studies of New and Sterilized Nickel-Titanium Rotary Endodontic Instruments”, Journal of Endodontics, vol. 32, no. 7, pp. 675-679, August 2006.

[20] Budynas−Nisbett ,“Shigley’s Mechanical Engineering Design” ed. Mc Graw Hill, eight edition, pp. 258 - 313.

[21] James H. Yao; Scott A. Schwartz; and Thomas J. Beeson, “Cyclic Fatigue of Three Types of Rotary Nickel-Titanium Files in a Dynamic Model”, *Journal of Endodontics*, vol. 32, no. 1, pp. 55-57, January 2006.

[22] Uei-Ming Li; Bor-Shiunn Lee; Chin-Tsai Shih; et. al., “Cyclic Fatigue of Endodontic Nickel Titanium Rotary Instruments: Static and Dynamic Tests”, Journal of Endodontics, vol. 28, no. 6, pp. 448-51, July 2002.

[23] Yehdua Zadik; Vadim Sandler; Ron Bechor; et. al., “Analysis of factors related to extraction of endodontically treated teeth”, Oral Surgery, Oral Medicine, Oral Pathology, Oral Radiology, and Endodontology, vol. 106, no. 5, pp. e31-e35, 2008

[24] Jesus Djalma Pécora; Julian B. Woelfel; andManoel Damião Sousa Neto, “Morphologic Study of the Maxillary Molars Part I: External Anatomy”, *Braz Dent J*,vol. 2, no. 1, pp. 45-50, 1991.

[25] Ove A. Peters; Andres Laib; Till N. Gohring; et. al., “Changes in Root Canal Geometry after Preparation Assessed by High-Resolution Computed Tomography”, *Journal of Endodontics,* vol. 27, no.1, pp. 1-6, January 2001.

[26] Pedro Santos, “Avaliação da resistência à fadiga de instrumentos endodônticos sujeitos a polimento electrolítico e a tratamento térmico específico”,pp 30 – 34, ed. FCT/UNL, 2014.

Annexes

Annex A - Hyflex™ CM Instruments

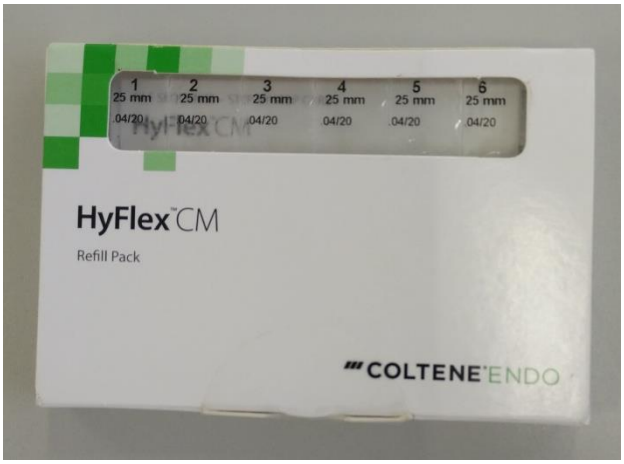

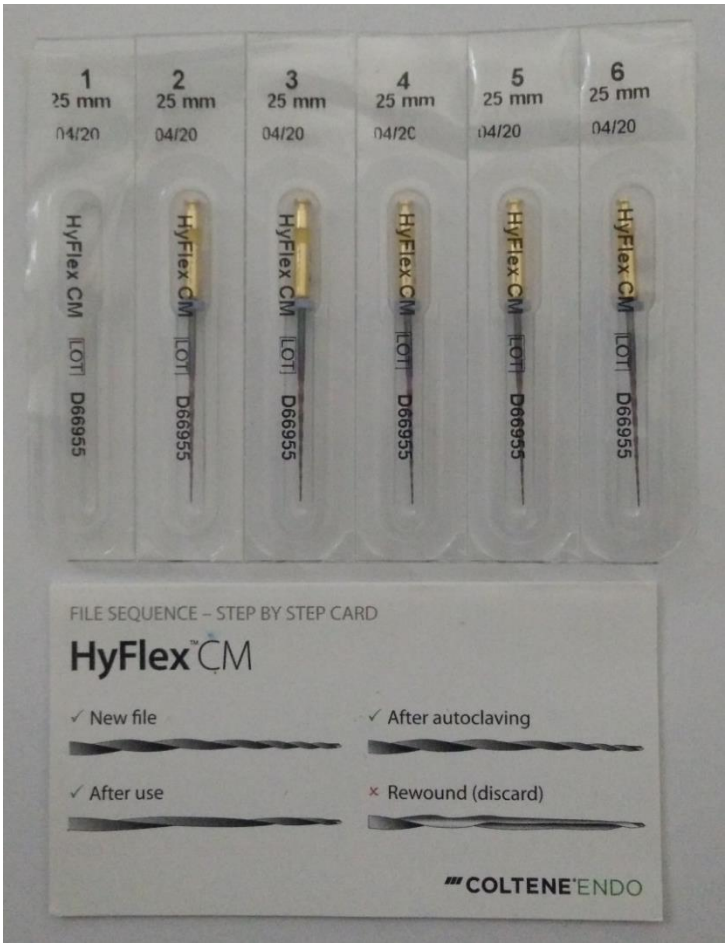

Annex B – Stepper motor and experimental setup images

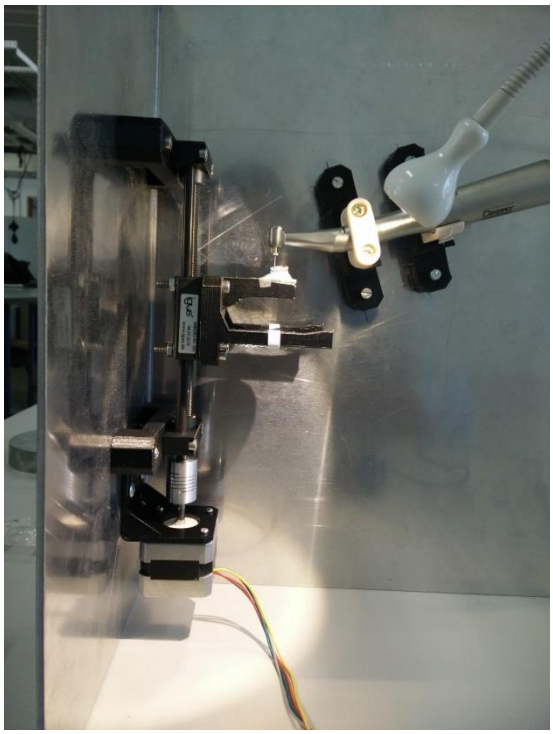

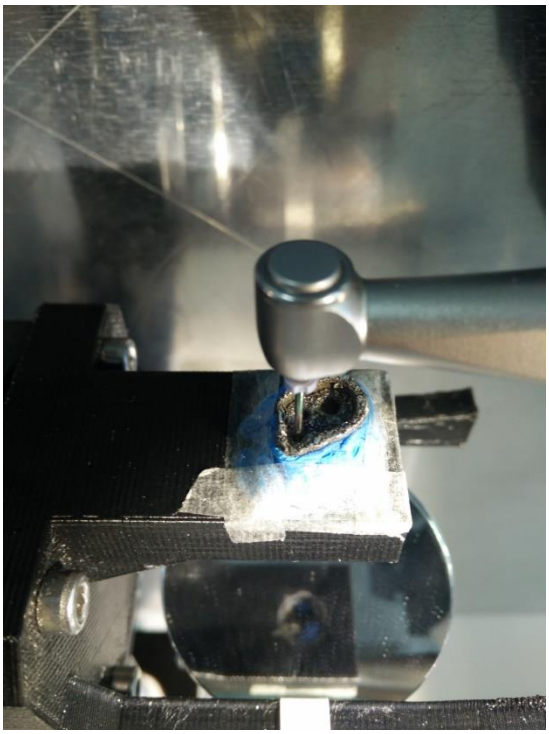

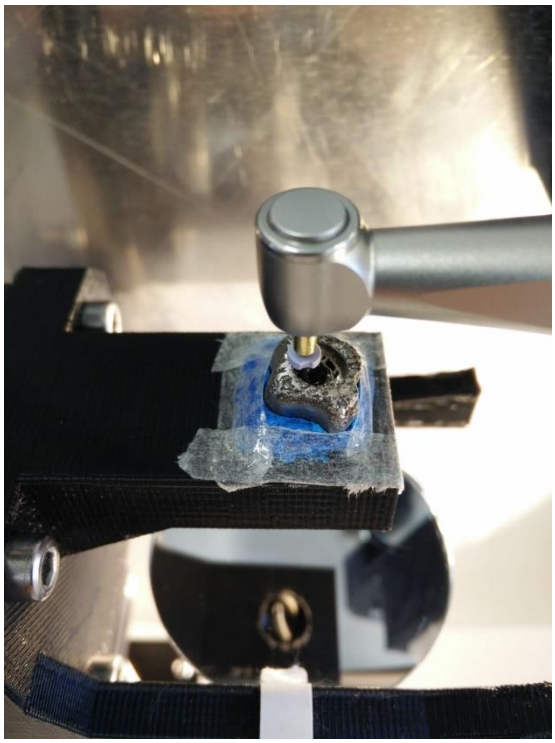

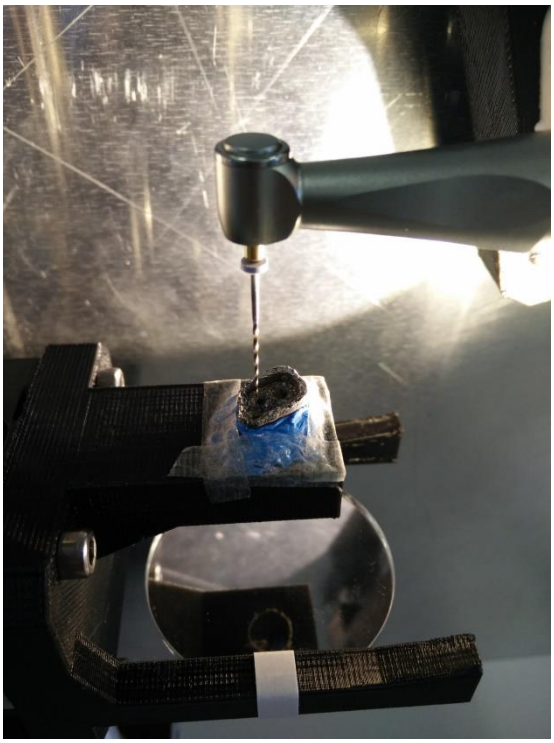

Annex C – Experimental setup with instrument failure pictures

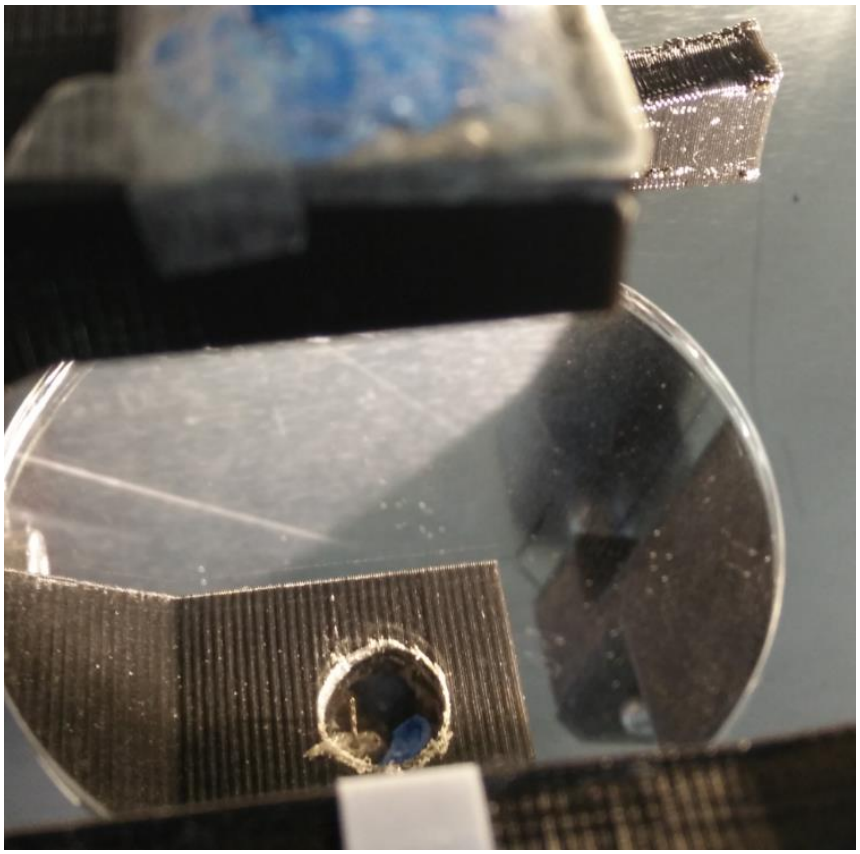

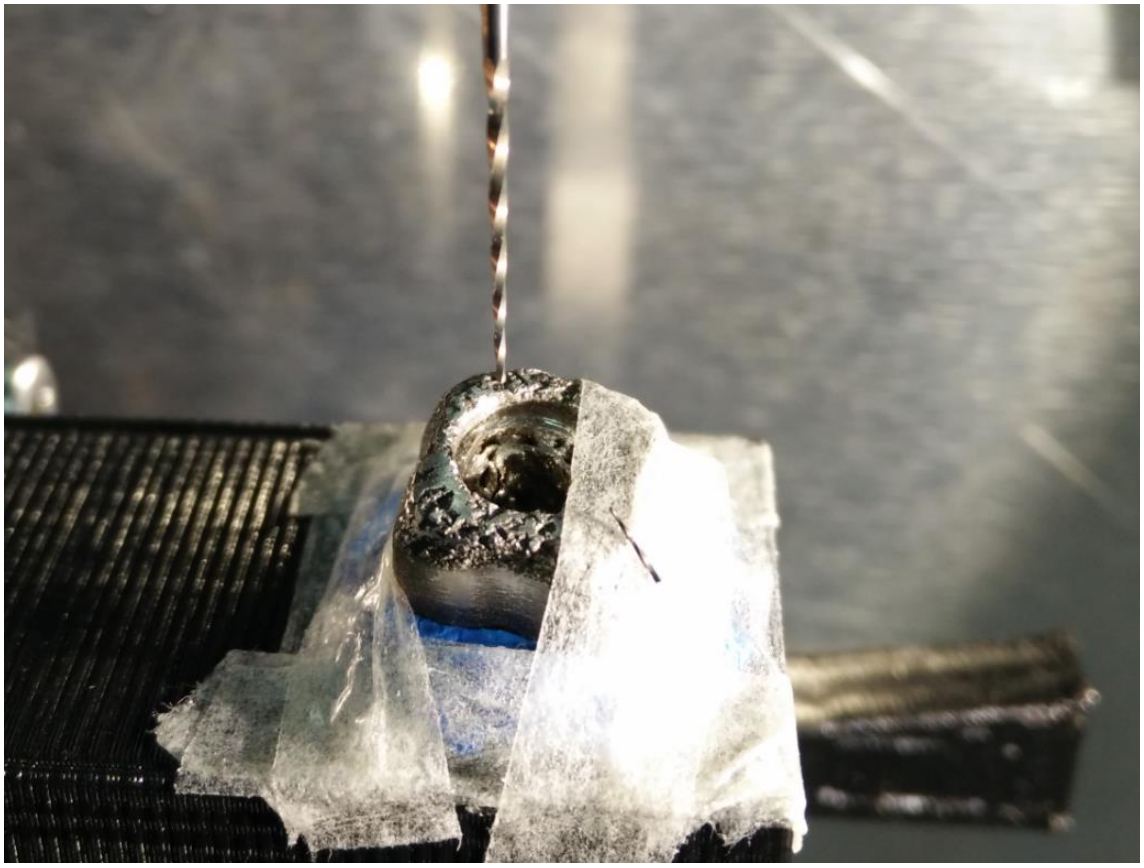

Annex D – Wave one picture

Annex E – Stepper motor and stepper motor control system pictures

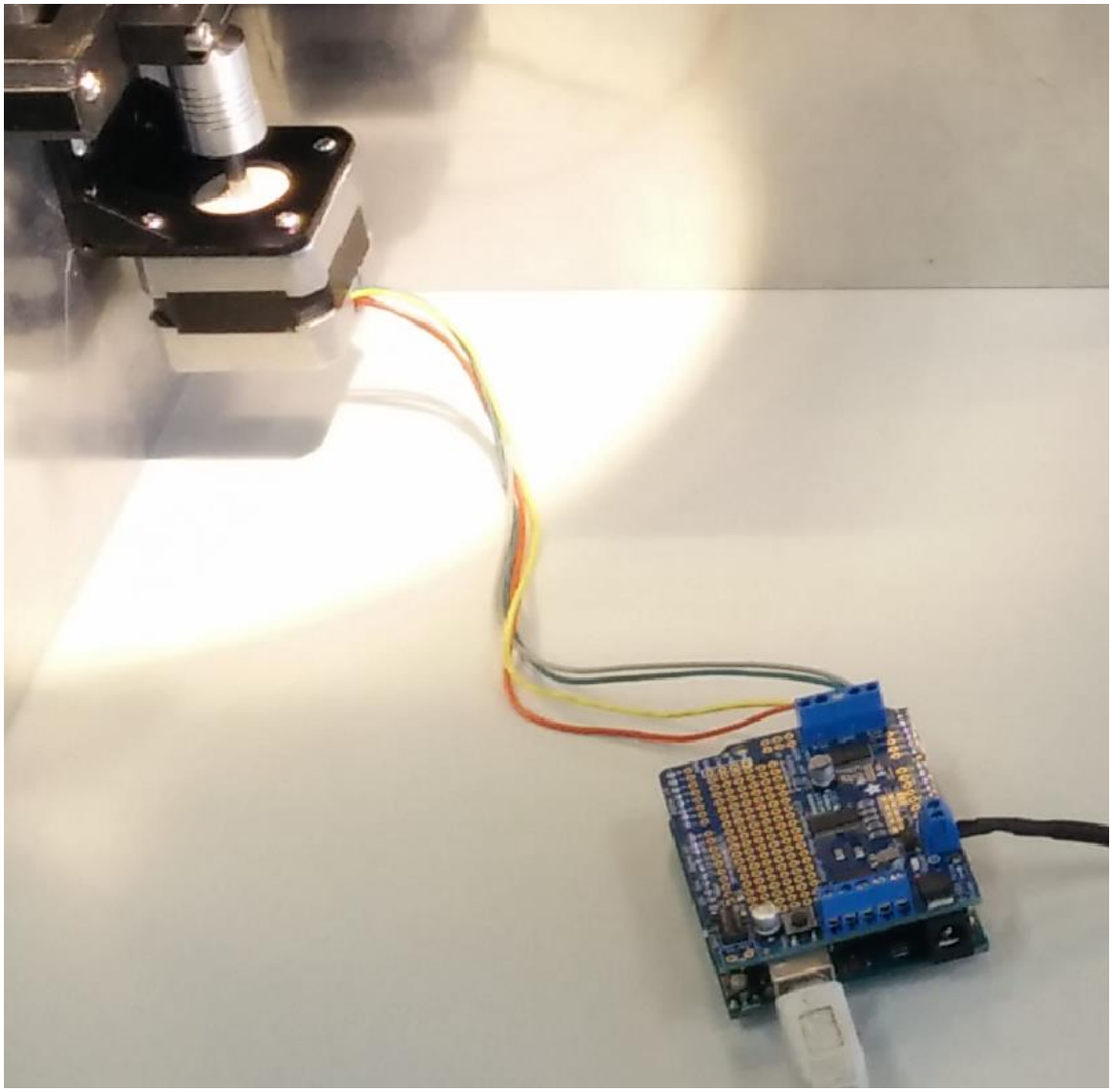

Annex F - Stepper motor datasheet

Adafruit NEMA-17

MODEL	SINGLE SHAFT	-951
DRIVE METHOD		BI-POLAR
NUMBER OF PHASES	———	2
STEP ANGLE	deg./step	1.8
VOLTAGE	V	12
CURRENT	A/PHASE	0.35
WINDING RESISTANCE	Ω /PHASE	34
INDUCTANCE	mH/PHASE	4.3
HOLDING TORQUE	mN • m	200
	oz • in	28
DETENT TORQUE	mN • m	11.8
	oz • in	2.1
ROTOR INERTIA	g • cm²	38
	oz • in²	0.21
WEIGHTS	g	200
	lb	0.57
INSULATION CLASS	———	JIS Class E (120°C 248°F) (UL VALUE : CLASS B-130°C 266°F)
INSULATION RESISTANCE	———	500VDC 100MΩmin.
DIELECTRIC STRENGTH	———	500VAC 50HZ 1min.
OPERATING TEMP. RANGE	°C	0 to 50
ALLOWABLE TEMP.RISE	deg.	70

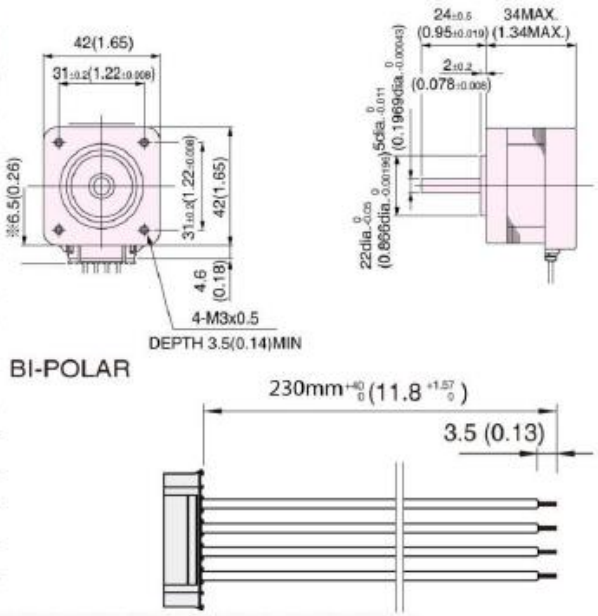

Annex G - Linear table datasheet

drylin® SHTP | Delivery Program | Trapezoidal Thread

drylin® SHTP linear drive technology

SHTP mini – Small and low-cost – Solid plastic

- Miniature version
- Very low weight
- Very low price
- Corrosion resistant
- Carriages and shaft end supports made of high performance polymers
- Available accessories
  ▶ page 1203

Order key

SHTP-01-06-AWM

- Shaft material
- Dimension
- Type
- SHT-Polymer

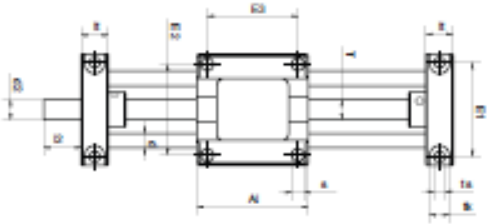

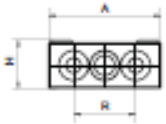

Technical Data

Part number	Max. length of stroke	Aluminum shaft		Max. static load-bearing capacity		more Information
		Weight	Additional [kg]	axial	radial	
	[mm]	[kg]	(per 100 mm)	[N]	[N]	
SHTP-01-06-AWM	300	0.11	0.06	50	50	Carriage, square, with four symmetrical mounting bores

Dimensions [mm]

Part number	A	Al	H	Ht	E1	E2	E3	l	R	f	kt	lt	tk	ts
SHTP-01-06-AWM	45	45	19	18	38	36.5	36.5	67	25	1	3	11	8	42

Part number	s	d	T	l2	d2*	ha
SHTP-01-06-AWM	5.1	6	M8	15	M8	9

* Standard versions supplied with lead screw end unmachined

delivery time 2–3 days

prices price list online www.igus.eu/eu/SHTP

Annex H - Arduino control program

The following control code runs in open loop on the Arduino Uno board and was written using the open source Arduino Software (IDE).

```
#include <Wire.h>
#include <Adafruit_MotorShield.h>
//includes the Adafruit motor shield library
// create the motor shield object with the default I2C address
Adafruit_MotorShield AFMS = Adafruit_MotorShield();
Adafruit_StepperMotor *myMotor = AFMS.getStepper(200, 2);
// Connect a stepper motor with 200 steps per revolution (1.8 degree)
// to motor port #2 (M3 and M4)


int val;
byte controlo;
byte go;

void setup() {
  Serial.begin(9600);
//Sets the data rate in bits per second 9600 baud
  AFMS.begin(1000);
 // create with the default frequency 1.0 KHz
  myMotor->setSpeed(144);
 //Sets the motor speed to 144 rpm to achieve a linear speed on the linear table of 3 mm/s, 1,25
// mm coarse pitch
}

void loop() {
  // creates a loop where the serial port is constantly being read
  while (Serial.available())
  {
    controlo = Serial.read();
  if (controlo=='1') {
// The motor makes 480 steps forwards and 480 steps backwards continuously by activating
//one pair of coils  at  time.
   myMotor->step(480, BACKWARD, DOUBLE);
   myMotor->step(480, FORWARD, DOUBLE);
   }
   else  {
     Serial.read();
      myMotor->step(0, BACKWARD, SINGLE);
}
}
}
```

Annex I – Control panel C# Form code

The Windows Form Application specifically designed to control the experimental axial motion mechanism was written in Visual C# through the Visual Studio Community 2015 RC with the DreamSpark agreement number: 1204026408.

```
using System;
using System.Collections.Generic;
using System.ComponentModel;
using System.Data;
using System.Drawing;
using System.Linq;
using System.Text;
using System.Threading.Tasks;
using System.Windows.Forms;
using System.IO.Ports;
using System.Threading;
using System.Diagnostics;
using Controlo_Motor_Loios;

namespace ControloMotor_Loios
{
   public partial class Form2 : Form
   {
//------------------------------------------------------------
// Creates the Stopwatch called stopwatch and the serial port as port, defines the Boolean
//variable keepGooing  as true and the integer a as -1
//------------------------------------------------------------
       Stopwatch stopWatch = new Stopwatch();
       bool keepGoing = true;
       int a = -1;
       SerialPort port;
       public Form2()
       {
//--------------------------------------
// Creation of some useful functions
//--------------------------------------
           InitializeComponent();
           ToggleState();
           init();
           Resultnumber();
       }
//--------------------------------------
// Definition of the Resultnumber() function
//--------------------------------------
       private void Resultnumber()
       {
           a = a + 1;
       }

       private void init()
       {
//--------------------------------------
// As soon as the program is loaded it tries to connect to the serial port COM 12 with a baud rate
//of 9600 bits/s, if unsuccessful it gives an error message
//--------------------------------------
           port = new SerialPort();
```

```
            port.PortName = "COM12";
            port.BaudRate = 9600;

            try
            {
                port.Open();
            }
            catch (Exception e1)
            {
                MessageBox.Show(e1.Message);
            }
        }


        private void button1_Click(object sender, EventArgs e)
        {
//----------------------------------------
// If button ON is pressed the stopwatch starts counting from 00:00:00 and the function Toggle
//state is called
//----------------------------------------
            ToggleState();
            StartCounting();
            stopWatch.Start();
            label1.Text = "00:00:00";
            button1.Text = "ON";
            MessageBox.Show("Please press the OFF button as soon as the instrument rupture
occurs");
        }

        private void button2_Click_1(object sender, EventArgs e)
        {
//----------------------------------------
// If button OFF is pressed the stopwatch stops counting, the togglestate function is called and
//the measured time is written on the text box
//----------------------------------------
            ToggleState();
            stopWatch.Stop();
            button2.Text = "OFF";
            MessageBox.Show("End of assessment");
            TimeSpan ts = stopWatch.Elapsed;
            string elapsedTime = String.Format("{0:00}:{1:00}:{2:00}.{3:00}",
                    ts.Hours, ts.Minutes, ts.Seconds,
                    ts.Milliseconds / 10);
            label1.Text = elapsedTime;
            Resultnumber();
            listBox1.Items.Add(a+"."+"   "+elapsedTime);
            stopWatch.Reset();
        }
        private void ToggleState()
        {
//----------------------------------
// The ToggleState function associates the button action to the boolean keepGoing variable,
//with the aim of switching between true and false
//----------------------------------
            keepGoing = !keepGoing;
            button1.Enabled = !keepGoing;
            button2.Enabled = keepGoing;
        }
        private void StartCounting()
        {
```

```
//---------------------------------
// Performs concurrent processing “Threading’’ to continuously send ‘’0’’ or ‘’1’’ digital signals
//through the port COM12 depending on the state of the boolean variable KeepGoing
//---------------------------------
            ThreadStart ts = new ThreadStart(Count);
            Thread t = new Thread(ts);
            t.Start();
        }

        private void Count()
        {
            while (keepGoing)
            {
                port.WriteLine("1");
            }
            port.DiscardOutBuffer();
            port.WriteLine("0");
            while (!keepGoing)
            {
                port.DiscardOutBuffer();
                port.WriteLine("0");
            }
        }

        private void menuStrip1_ItemClicked(object sender, ToolStripItemClickedEventArgs e)
        {

        }

        private void exitToolStripMenuItem1_Click(object sender, EventArgs e)
        {
            Application.Exit();
        }

        private void fileToolStripMenuItem_Click(object sender, EventArgs e)
        {
            this.Close();
        }
    }
}
```

Annex J – Pictures of the ANDREX Constant Potential X-Ray Set

Annex K – Front and top views of three endodontic instruments tested

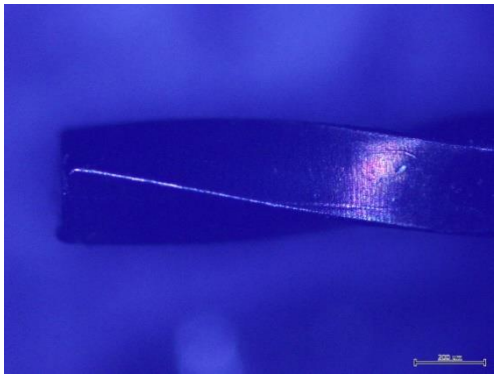

Instrument ref. 04/20_1: coronal, axial static

Magnification = 50x, front view

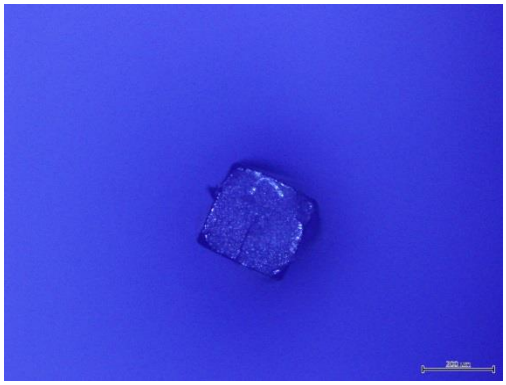

Instrument ref. 04/20_1: coronal, axial static

Magnification = 50x, top view

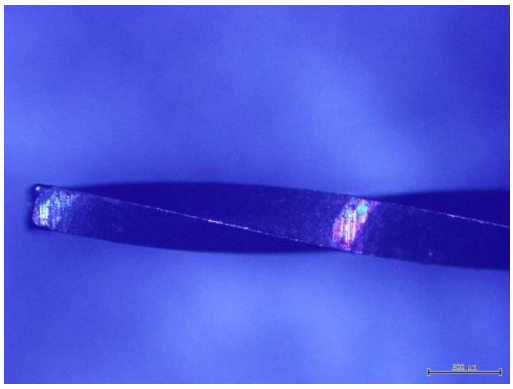

Instrument ref. 04/20_9: apical, dynamic

Magnification = 50x, front view

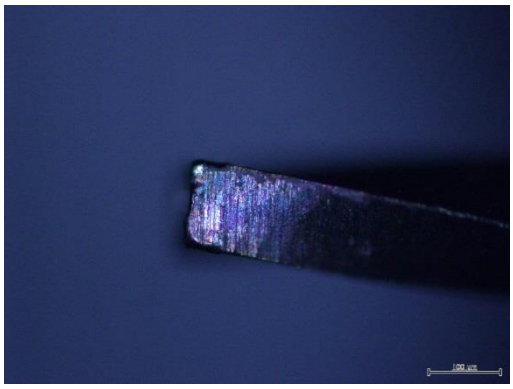

Instrument ref. 04/20_9 apical, dynamic

Magnification = 100x, front view

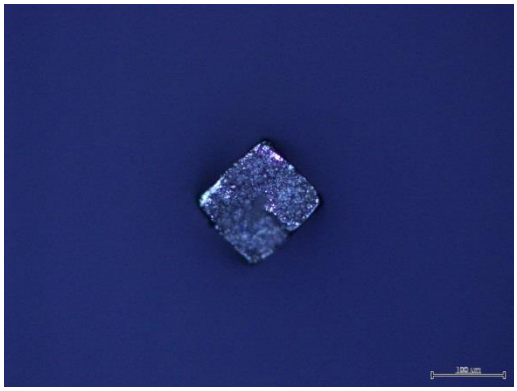

Instrument ref. 04/20_9 apical, dynamic

Magnification=100x, top view

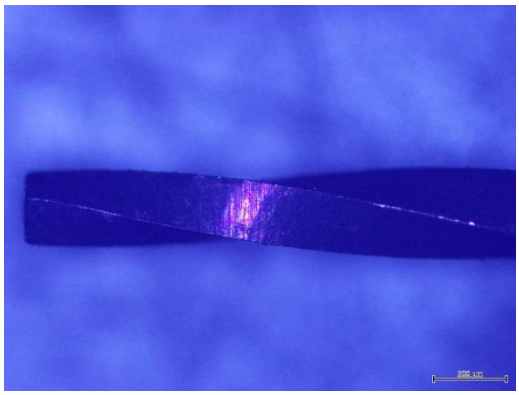

Instrument ref. 04/20_12: apical, axial static

Magnification=50x, front view

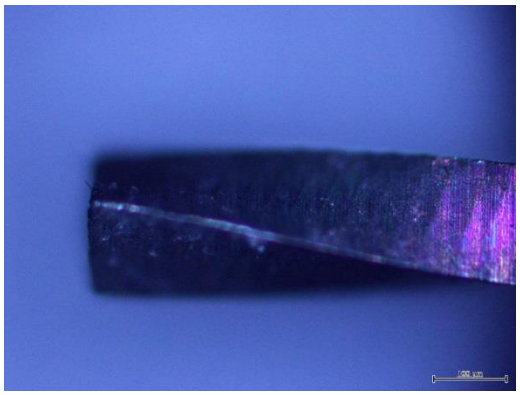

Instrument ref. 04/20_12 apical, axial static

Magnification=100x, front view

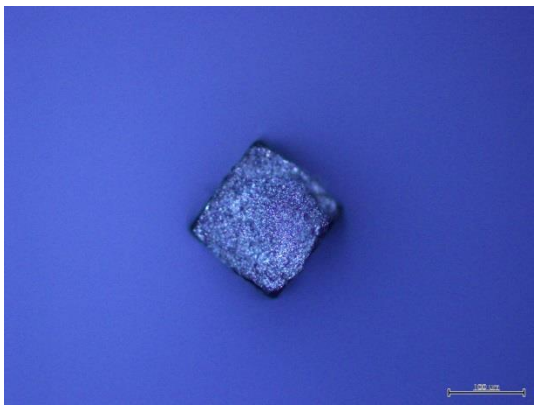

Instrument ref. 04/20_12 apical, axial static

Magnification=100x, top view

Annex L – Technical draws of the experimental setup